# Fluorescent H₂ Emission Lines from the Reflection Nebula NGC 7023 Observed with IGRINS

Huynh Anh N. Le[1,2], Soojong Pak[1], Kyle Kaplan[3], Gregory Mace[3], Sungho Lee[4], Michael Pavel[3], Ueejeong Jeong[4], Heeyoung Oh[2,4], Hye-In Lee[1], Moo-Young Chun[4], In-Soo Yuk[4], Tae-Soo Pyo[5,6], Narae Hwang[4], Kang-Min Kim[4], Chan Park[4], Jae Sok Oh[4], Young Sam Yu[4], Byeong-Gon Park[4], Young Chol Minh[4], and Daniel T. Jaffe[3]

[1] School of Space Research, Kyung Hee University, 1732 Deogyeong-daero, Giheung-gu, Yongin-si, Gyeonggi-do 17104, Korea; huynhanh7@khu.ac.kr, soojong@khu.ac.kr
[2] Department of Physics and Astronomy, Seoul National University, 1 Gwanak-ro, Gwanak-gu, Seoul 08826, Korea
[3] Department of Astronomy, University of Texas at Austin, Austin, TX 78712, USA
[4] Korea Astronomy and Space Science Institute, Daejeon 34055, Korea
[5] Subaru Telescope, National Astronomical Observatory of Japan, National Institutes of Natural Sciences (NINS), 650 North Aohoku Place, Hilo, HI 96720, USA
[6] School of Mathematical and Physical Science, SOKENDAI (The Graduate University for Advanced Studies), Hayama, Kanagawa 240-0193, Japan

## Abstract

We have analyzed the temperature, velocity, and density of H₂ gas in NGC 7023 with a high-resolution near-infrared spectrum of the northwestern filament of the reflection nebula. By observing NGC 7023 in the $H$ and $K$ bands at $R \simeq 45,000$ with the Immersion GRating INfrared Spectrograph, we detected 68 H₂ emission lines within the $1'' \times 15''$ slit. The diagnostic ratio of 2-1 S(1)/1-0 S(1) is $0.41-0.56$. In addition, the estimated ortho-to-para ratio (OPR) is $1.63-1.82$, indicating that the H₂ emission transitions in the observed region arise mostly from gas excited by UV fluorescence. Gradients in the temperature, velocity, and OPR within the observed area imply motion of the photodissociation region (PDR) relative to the molecular cloud. In addition, we derive the column density of H₂ from the observed emission lines and compare these results with PDR models in the literature covering a range of densities and incident UV field intensities. The notable difference between PDR model predictions and the observed data, in high rotational $J$ levels of $\nu = 1$, is that the predicted formation temperature for newly formed H₂ should be lower than that of the model predictions. To investigate the density distribution, we combine pixels in $1'' \times 1''$ areas and derive the density distribution at the 0.002 pc scale. The derived gradient of density suggests that NGC 7023 has a clumpy structure, including a high clump density of $\sim 10^5$ cm$^{-3}$ with a size smaller than $\sim 5 \times 10^{-3}$ pc embedded in lower-density regions of $10^3$–$10^4$ cm$^{-3}$.

*Key words:* infrared: ISM – ISM: individual objects (NGC 7023) – ISM: molecules – ISM: kinematics and dynamics – photon-dominated region (PDR) – techniques: spectroscopic

## 1. Introduction

Molecular hydrogen H₂ is a major component of the interstellar medium (ISM). Rovibrational H₂ emission lines arise either in shock-heated regions or in photodissociation regions (PDRs). In PDRs, the far-UV (FUV) photons illuminate the transition layer between the ionized gas and the surface of the molecular cloud (Tielens & Hollenbach 1985a, 1985b; Black & Van Dishoeck 1987; Burton et al. 1989; Sternberg & Dalgarno 1989; Draine & Bertoldi 1996; Luhman et al. 1997; Hollenbach & Tielens 1999). Molecular hydrogen emission has been observed in reflection nebulae (e.g., NGC 2023: Sellgren 1986; Gatley et al. 1987; Hasegawa et al. 1987; Burton et al. 1998; Martini et al. 1999; McCartney et al. 1999; Habart et al. 2004, 2011; Fleming et al. 2010; Sheffer et al. 2011), the Orion nebula (Hayashi et al. 1985; Luhman & Rieke 1996; Luhman et al. 1998; Bertoldi et al. 1999; Rosenthal et al. 2000; Habart et al. 2004; Allers et al. 2005), M17 (Chrysostomou et al. 1992, 1993; Sheffer & Wolfire 2013), and in planetary nebulae (e.g., Hubble 12: Ramsay et al. 1993; Hora & Latter 1996; Chrysostomou et al. 1998; Marquez-Lugo et al. 2015).

In general, H₂ emission lines at $\nu = 0$ and low rotational $J$ levels are good indicators of the gas temperature in the layer where they arise, while H₂ lines arising from higher excitation energy states are pumped by UV photons and are sensitive to the radiation field, gas temperature, and gas density.

Theoretical PDR models predict the intensities and line ratios of H₂ in PDRs well (Sternberg & Dalgarno 1989; Draine & Bertoldi 1996; Shaw et al. 2004, 2009). However, observations of rotational H₂ emission lines by *ISO* (the *Infrared Space Observatory*, Kessler et al. 1996) indicate that the gas temperature derived from initial rotational levels of H₂ is higher than that predicted in the PDR models (Timmermann et al. 1996; Bertoldi et al. 1999; Draine & Bertoldi 1999; Fuente et al. 1999; Thi et al. 1999). Theoretical models have difficulty explaining the existence of much warmer H₂ rotational emission zones. Modification of the heating and cooling processes, or H₂ formation rates, has been proposed to explain these discrepancies (Draine & Bertoldi 1999; Habart et al. 2004; Allers et al. 2005). Weingartner & Draine (1999) suggested that radiation forces on dust grains can enhance the dust-to-gas ratio, thus increasing the gas-heating rate.

Discrepancies between the observed intensities of fluorescent H₂ emission from highly excited energy levels, or high rotational states, and those predicted by PDR models, are a source of debate. Burton et al. (1998) indicated that the observed intensities of high $\nu$ lines are weaker than model predictions. Yet, Bertoldi et al. (2000) pointed out that the observed intensities of H₂ emission lines at very high energy states ($\nu = 9$ and 12) were stronger than the values predicted by their PDR model. In addition, H₂ lines arising from high-$\nu$ or high-$J$ states are sensitive to UV field intensity and gas
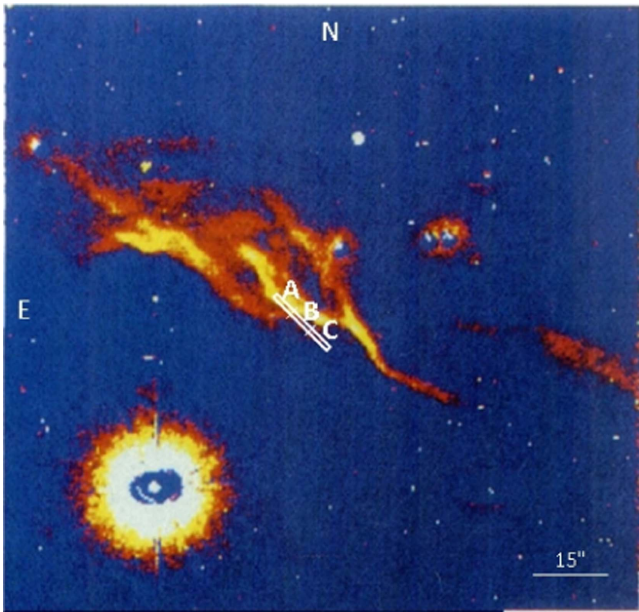
**Figure 1.** Image of the $H_2$ emission at 2.121 $\mu$m from the northwestern filament of NGC 7023 recorded in Lemaire et al. (1996). In the image, the central illuminating star, HD 200775, lies at $\alpha(2000) = 21^h01^m36\overset{s}{.}9$ and $\delta(2000) = 68°09'47\overset{''}{.}8$. The IGRINS slit center position is located at $29\overset{''}{.}0$ west, $32\overset{''}{.}7$ north of the star with PA = 45°. The positions of regions A, B, and C are shown as text in the image.

density. The difference between model results and observations may be explained by the effects of collisional de-excitation of the UV-excited $H_2$, the formation of $H_2$, or changing ortho-to-para ratios (OPRs; Burton et al. 1998). Burton et al. (1992) suggested that $H_2$ formation has a significant effect on the $\nu = 4$ level from observations of NGC 2023 but the level distribution of newly formed $H_2$ is unclear (Draine & Bertoldi 1996; Bertoldi et al. 1999). To date, most of the observations of fluorescently excited $H_2$ emission lines have been taken at low spatial and spectral resolution. Those spectra do not have enough resolution to robustly test $H_2$ line intensities. At high spatial and spectral resolution, $H_2$ emission lines resolve the physical structure of PDRs and test the predictions and assumptions of fluorescent PDR models.

The reflection nebula NGC 7023 is illuminated by the Herbig B3Ve−B5 star HD 200775 (Witt et al. 2006; Alecian et al. 2008, 2013), with an effective temperature of 17,000 K (Baschek et al. 1982), at a distance of $430^{+160}_{-90}$ pc (van den Ancker et al. 1997). The proximity of this object to us and the known properties of the exciting star make it one of the best objects for studying PDRs. Observations show that this nebula hosts different gas density structures, including dense clumps ($n \sim 10^6$ cm$^{-3}$) embedded in lower-density gas ($n = 10^4$–$10^5$ cm$^{-3}$) (Chokshi et al. 1988; Sellgren et al. 1992; Fuente et al. 1996, 2000; Lemaire et al. 1996; Martini et al. 1997, 1999; Takami et al. 2000; An & Sellgren 2003; Fleming et al. 2010; Habart et al. 2011; Pilleri et al. 2012a, 2012b; and Köhler et al. 2014). At the wall of the cavity, PDR emission arises $\sim42''$ northwest, $\sim55''$ southwest, and $\sim155''$ east of the central illuminating star where the FUV field intensities of $G = 2600, 1500,$ and 250, respectively, in units of $G_0 = 1.6 \times 10^{-3}$ erg cm$^{-2}$ s$^{-1}$ (Pilleri et al. 2012b).

NGC 7023 has been observed in the near-infrared (near-IR) by many authors (e.g., Sellgren 1986; Sellgren et al. 1992; Lemaire et al. 1996, 1999; Martini et al. 1997, 1999). In particular, low spectral resolution observations of $H_2$ emission

(Martini et al. 1997, 1999) found high-density clumps in the PDR regions of NGC 7023. In addition, Lemaire et al. (1996) found small-scale structure, less than 0.004 pc, based on high spatial resolution images of $\nu = 1$-0 S(1) and S(2) rovibrational lines.

The Immersion Grating Infrared Spectrograph (IGRINS) covers the entire $H$ and $K$ bands (1.4–2.5 $\mu$m) in a single exposure, with a resolving power of $R \simeq 45,000$ (Yuk et al. 2010; Park et al. 2014). Since its commissioning in 2014, many interesting results in the ISM have been explored by various authors (Lee et al. 2015; Afşar et al. 2016; Oh et al. 2016a, 2016b; Lee et al. 2016; Sterling et al. 2016; Kaplan et al. 2017).

With our IGRINS observations we can isolate the physical structure and properties in the observed region with high spectral and spatial resolutions, and study many $H_2$ transitions simultaneously with an exact spatial registration of the observations at different wavelengths. In this paper, we present detections of many $H_2$ lines from the northwestern (NW) filament of NGC 7023 and derive the distribution of the temperature, column density, and OPR of $H_2$ in the observed area. We also test the reliability of PDR models at the H II and $H_2$ interface in NGC 7023.

## 2. Observations and Data Reduction

### 2.1. Observations

We observed NGC 7023 on 2014 July 12 during IGRINS commissioning on the 2.7 m Harlan J. Smith Telescope at the McDonald Observatory. The slit position angle was 45° (east from north) for this observation and the slit size was fixed at $1'' \times 15''$. The slit center position (SC) in the nebula was $29\overset{''}{.}0$ west, $32\overset{''}{.}7$ north of the central illuminating star, HD 200775, which lies at $\alpha(2000) = 21^h01^m36\overset{s}{.}9$ and $\delta(2000) = 68°09'47\overset{''}{.}8$. We use the "Nod-off-slit" mode with an "off" position $120''$ to the north from the target. The total on-source exposure time was 1200 s. Figure 1 shows the position of the slit on an $H_2$ 2.121 $\mu$m emission map (Lemaire et al. 1996). Based on the FWHM of the bright star in the slit-view camera image of NGC 7023, the seeing during the observation was $\sim1\overset{''}{.}0$ in the $K$ band.

### 2.2. Data Reduction

Data reduction was performed using the IGRINS data reduction pipeline package[7] (Lee 2015). The standard data reduction processes, including bad-pixel and cosmic ray correction, flat fielding, sky subtraction, spectral extraction, and wavelength calibration, are described in Sim et al. (2014). We corrected bad pixels and cosmic rays for all of the target and sky frames. A combined master flat image was made to correct variations from pixel-to-pixel in the detector and to do aperture extraction maps for tracing the orders in the echellogram. Thorium–argon (ThAr) emission lines were used to perform distortion correction and wavelength calibration. The sky background was corrected by subtracting the sky frame from the target frame. Telluric absorption correction and absolute flux calibration was achieved by dividing by the spectrum of the A0V standard star HD 155379 observed at a similar airmass to NGC 7023.

---

[7] See also the IGRINS pipeline package at https://github.com/igrins/plp/tree/v2.0.
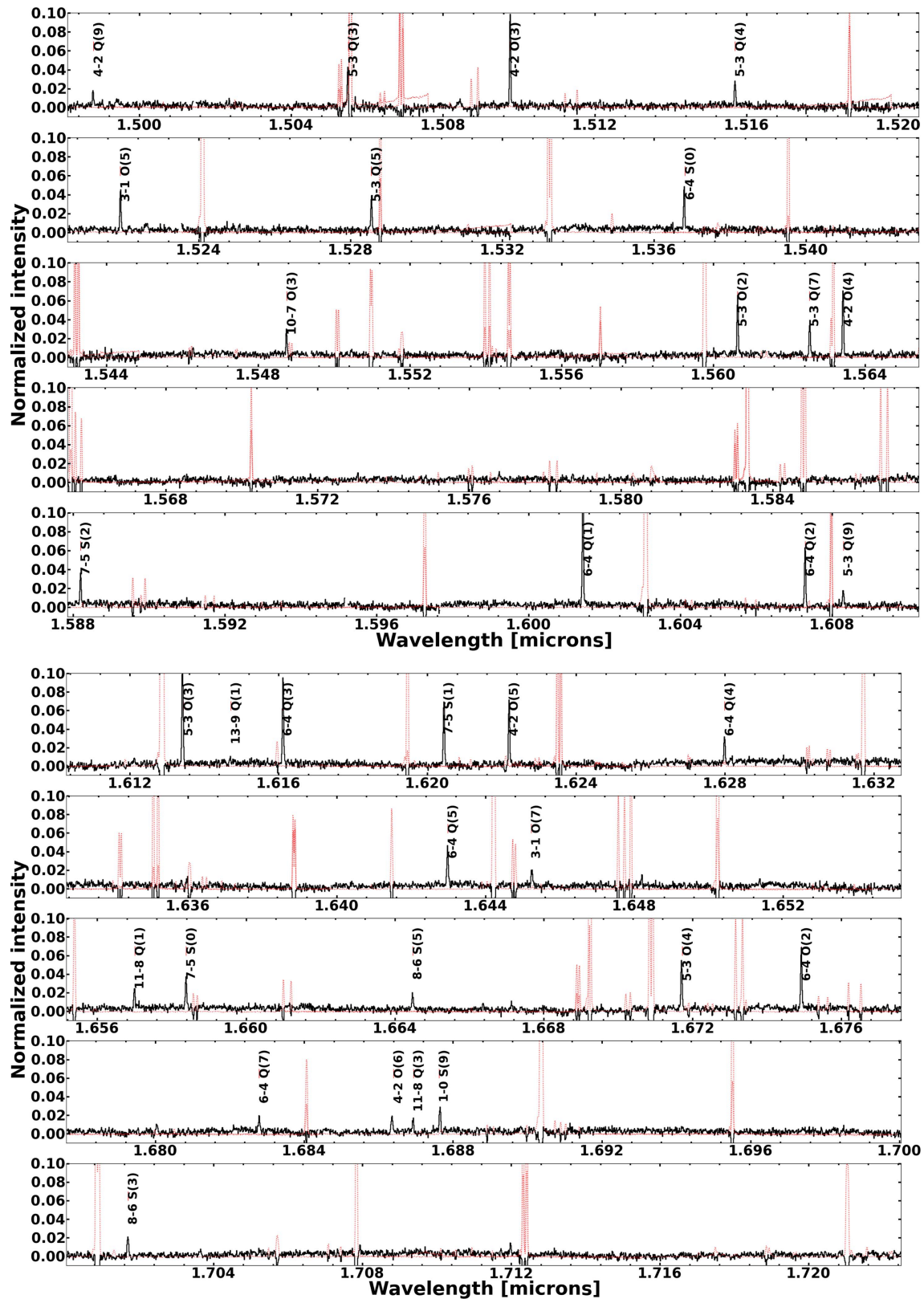
**Figure 2.** *H*- and *K*-band spectra from the NW filament of NGC 7023. The intensity has been normalized by the peak of the 1-0 S(1) line. The normalized intensity of H$_2$ 1-0 S(1) 2.1218 $\mu$m is one. We marked the identified lines with their names in the figure. The red dashed lines display OH emission lines, observed at "off" position 120″ to the north from the target.
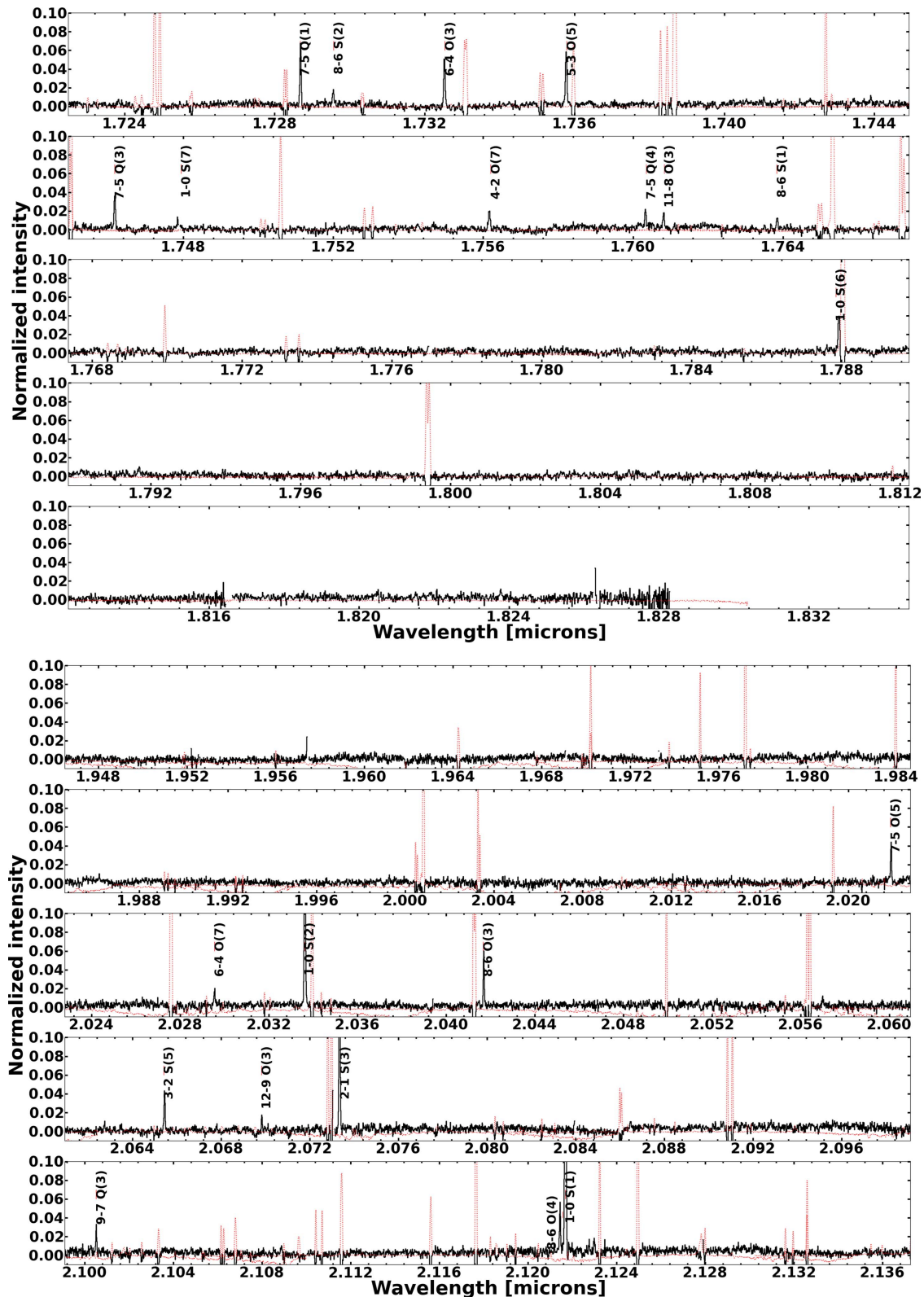
3

**Figure 2.** (Continued.)

### 2.3. $H_2$ Line Collection and OH-residuals

OH lines cannot be completely removed from the target frame because telluric OH line fluxes vary over time. Residual OH emission lines may be misidentified as $H_2$ lines or disturb the identified lines. Figure 2 shows the whole spectrum from the NW filament of NGC 7023 with the intensity values
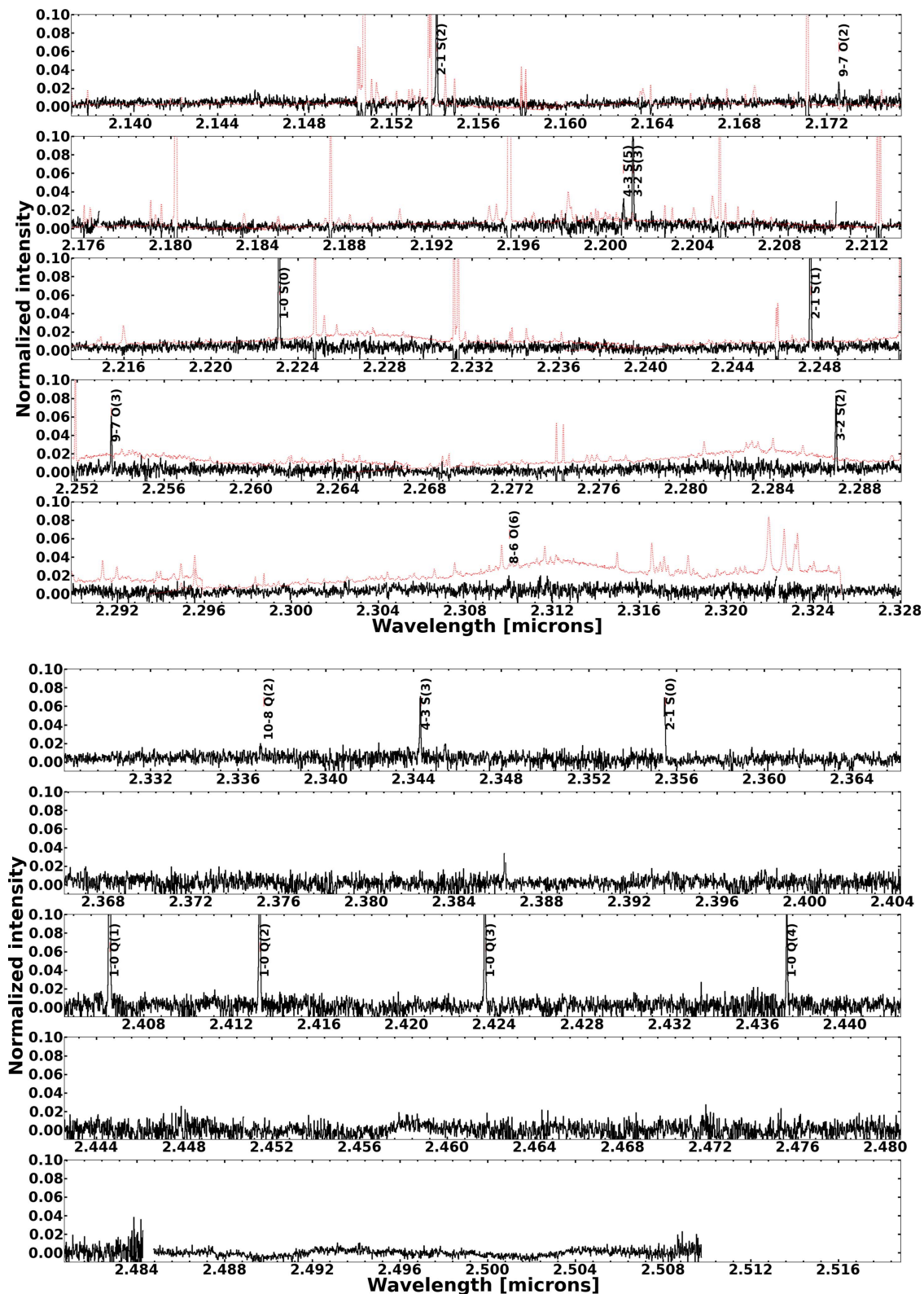
**Figure 2.** (Continued.)

normalized to the 1-0 S(1) intensity. All of the identified lines are marked in the figures. We used the list of wavelengths of $H_2$ transitions in Draine & Bertoldi (1996), and detected 68 $H_2$ rovibrational emission lines. In addition, we also overplot the

OH airglow emission lines in the off-position spectra in Figure 2 to check whether the $H_2$ lines are contaminated by OH-residuals or not. We carefully checked the measured wavelength of the detected lines by comparing with the

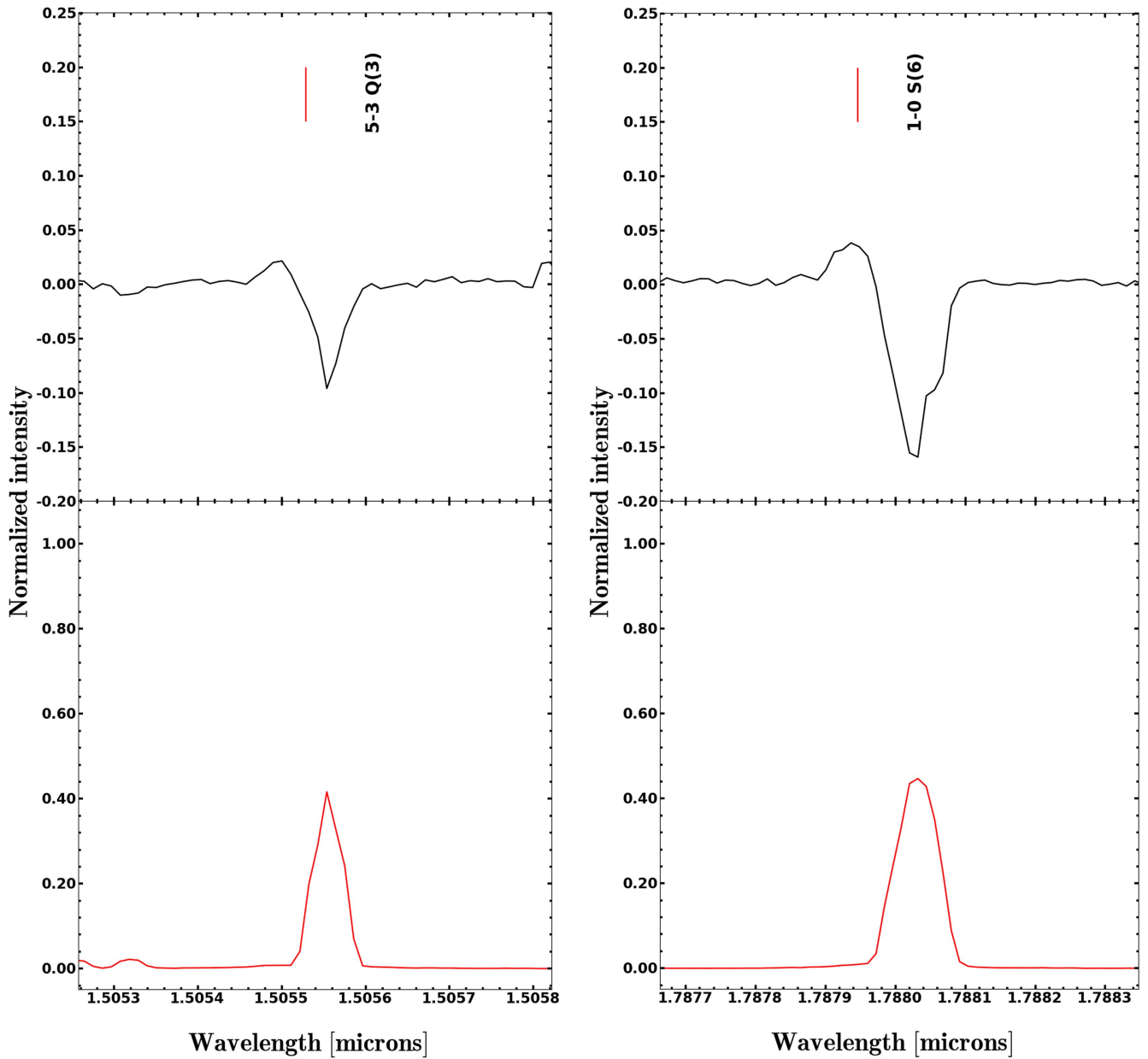**Figure 3.** Observed $H_2$ 5-0 O(3) and 1-0 S(6) line profiles (black solid lines). The intensity has been normalized by the peak of the 1-0 S(1) line. The OH emission lines (red solid lines) are shown in the bottom plots.

published wavelength of the OH lines in $H$ and $K$ band spectra (Rousselot et al. 2000). Then, we confirm that the $H_2$ line identifications are reliable. In the cases of 5-3 Q(3) and 1-0 S(6), we note that those lines are blended since they are strongly disturbed by OH-residuals after a subtraction of the OH emission lines. Figure 3 shows the observed 5-3 Q(3) and 1-0 S(6) line profiles.

## 3. Analysis

### 3.1. Flux Calibration

We measured and calibrated the intensity using the methods in Le et al. (2015). We integrate the source signal within $\pm 12\,\mathrm{km\,s^{-1}}$ of the line center, because the typical

observed full width at half maximum (FWHM) of the detected $H_2$ lines is $\sim 8\,\mathrm{km\,s^{-1}}$ (dominated by instrument line width). The noise was estimated by combining the source noise from the line flux itself with the detector read noise in quadrature.

The flux calibration is done by converting pixel values in ADU into specific intensities in physical units (e.g., $\mathrm{W\,m^{-2}\,arcsec^{-2}}$), for which we follow the methods in Lee & Pak (2006). By calculating the flux calibration scaling factor $\mathfrak{R}_{\mathrm{ext}}$, the flux calibration is determined by,

$$I(\lambda) = \mathfrak{R}_{\mathrm{ext}}(\lambda) S(\lambda), \qquad (1)$$

where $I(\lambda)$ is specific intensity in units of $\mathrm{W\,m^{-2}\,\mu m^{-1}\,arcsec^{-2}}$, and $S(\lambda)$ is in ADU units. The scaling factor of flux
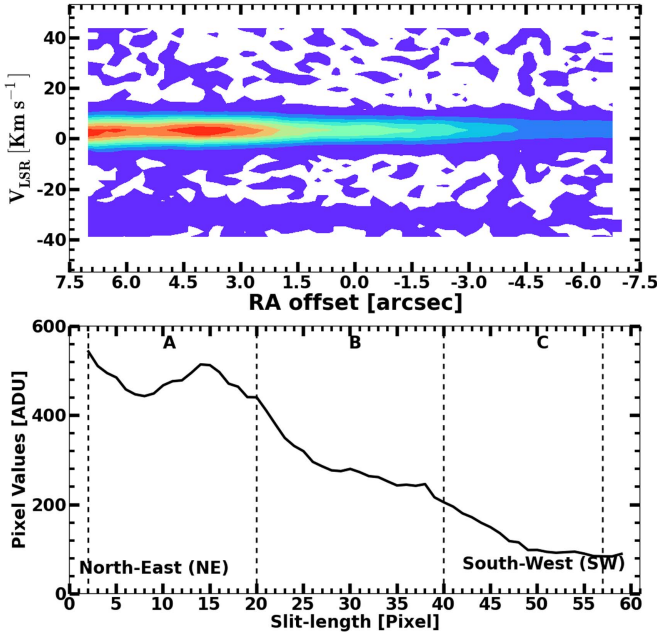
**Figure 4.** Radial velocity diagram of the 1-0 S(1) line (top plot). In the diagram, $1'' = 3.66$ pixels. The bottom plot shows the intensity profile at the peak of the 1-0 S(1) line. The black dashed lines show the separated regions A, B, and C along the slit length.

calibration $\mathfrak{R}_{\mathrm{ext}}$ is calculated by,

$$\mathfrak{R}_{\mathrm{ext}}(\lambda) = \frac{F_{\mathrm{std}}(\lambda)}{S_{\mathrm{std}}(\lambda)} \frac{1}{\Omega} \frac{t_{\mathrm{std}}}{t_{\mathrm{obj}}} \frac{1}{W_{\mathrm{slit}} \tau_{\mathrm{slit}}}, \quad (2)$$

where $F_{\mathrm{std}}$ is the flux density of the standard star HD 155379 in W m$^{-2}$ $\mu$m$^{-1}$ with a K-magnitude of $m_k = 6.52$ mag, $S_{\mathrm{std}}(\lambda)$ is the integrated pixel value of the standard star in ADU units, $\Omega = 0''.27 \times 0''.27$ arcsec$^2$ is the field-of-view (FOV, 1 pixel $= 0''.27$), $t_{\mathrm{std}} = 480$ s and $t_{\mathrm{obj}} = 1200$ s are the exposure time of the standard star and the object, respectively, and $W_{\mathrm{slit}} = 3.66$ pixels is the width of the slit. Note that there is a typo in Equation (8) of Lee & Pak (2006). The slit obscuration factor $\tau_{\mathrm{slit}}$ should be

$$\tau_{\mathrm{slit}} = \frac{1}{\mathrm{erf}\left(\frac{Y}{\sqrt{2}\sigma}\right)}, \quad (3)$$

where $Y$ is half of the slit width, $Y = 0''.5$, and $\sigma$ is the Gaussian width of the point-spread function (PSF) along the slit length. The measured $\sigma$ in our IGRINS spectrum is $0''.84$.

### 3.2. $H_2$ Spectra

Figure 4 shows a position-radial velocity diagram of the $H_2$ 1-0 S(1) line. The peak intensity profile of the line is also displayed. We divided the observed region along the slit length from north–east (NE) to south–west (SW) into regions of A (offset $7''.5 - 2''.5$ to the NE from SC), B (offset $2''.5$ to the NE and $2''.5$ to the SW from SC), and C (offset $2''.5 - 7''.5$ to the SW from SC).

We measured the intensity of 68 $H_2$ rovibrational emission lines arising in vibrational ladders from $\nu = 1$–13 and from rotational upper states as high as $J = 11$. For regions A, B, and

C we find that the upper states span an excitation temperature range of $E/k = 6100$–50,000 K.

In order to correct the measured intensity values of $H_2$ emission lines for dust extinction, we applied a visual extinction of $A_V = 2.2$ mag, derived from $R_V = 5$ (Mathis 1990) and $E(B - V) = 0.44$ (Witt & Cottrell 1980) as adopted by Martini et al. (1997, 1999). We also used the IR extinction law in Equation (4) (Cox 2000 and references therein) to correct for extinction across the entire IGRINS spectral range:

$$A(\lambda) = 0.412 A_V \lambda^{-1.75}. \quad (4)$$

Table 1 shows the $H_2$ intensities, listing only those lines with signal-to-noise greater than 5. Note that the real extinction values could be different from the adopted $A_V$, which we used to correct the intensity values of $H_2$ emission lines. This difference may affect our intensity measurements. We will discuss the effects that the adopted extinction values have on our results in the discussion section.

### 3.3. Dynamical Information from $H_2$ Lines

In Table 2, we present the line widths and velocities of the detected $H_2$ lines. Since we expect telluric absorption and OH airglow emission lines to contaminate our target spectra, we calculated the average velocity shift and line width of the detected $H_2$ emission lines and used those values as a reference for filtering the detected emission lines. We assume that all lines are from the same region and that reliable $H_2$ emission lines have velocities and line widths within the standard deviation of the detected emission lines, $\sigma_{V_{\mathrm{shift}}}$ and $\sigma_{V_{\mathrm{obs}}}$. The line shifts in wavelength locations have been corrected for the Earth and heliocentric velocities (8.63 km s$^{-1}$) and the local standard of rest velocity (LSR, 13.89 km s$^{-1}$), obtained by using the RVCORRECT task from IRAF.[8]

The radial velocities in $V_{\mathrm{LSR}}$ of the $H_2$ emission lines are 2–5 km s$^{-1}$. The average $V_{\mathrm{LSR}}$ of the $H_2$ lines for regions A, B, and C are $3.64 \pm 0.16$ km s$^{-1}$, $3.46 \pm 0.11$ km s$^{-1}$, and $3.39 \pm 0.22$ km s$^{-1}$, respectively. The average from all three regions is $3.50 \pm 0.16$ km s$^{-1}$, in agreement with the radial velocity of the 1-0 S(1) line given by Lemaire et al. (1999) for NGC 7023 at the position which is $\sim 5''$ offset from ours.

With the high spectral resolution of IGRINS, we were able to deconvolve the instrument profile from the $H_2$ emission lines. The measured FWHM was 7–9 km s$^{-1}$. Based on a comparison of the measured profiles of unresolved lines from our discharge ThAr arc calibration lamp, we found that a Gaussian is a good approximation to the instrumental profile. We therefore assume that the profile is Gaussian when deconvolving the spectra. We measured the line width of the ThAr emission lines from an internal IGRINS calibration lamp, observed from the same-night observations, and we used them as the line width of the instrument profile. We estimated the FWHM of the $H_2$ lines by subtracting in quadrature the instrumental profile determined from the same-night calibration measurements of a ThAr emission line spectrum.

Figure 5 shows one example of the $H_2$ 1-0 S(1) line, the instrument profile, and the Gaussian fit by deconvolving the instrument profile from the 1-0 S(1) line in region A. The derived intrinsic line width is 2–6 km s$^{-1}$. We found that the average line widths of regions A, B, and C were $4.63 \pm$

---

[8] IRAF (Image Reduction and Analysis Facility) is distributed by the National Optical Astronomy Observatories (NOAO).

**Table 1**
NGC 7023 $H_2$ Line Observation

| Line | $\lambda$[a] | Region A | | | Region B | | | Region C | | |
|------|------|---------|---------|----------------|---------|---------|----------------|---------|---------|----------------|
| | | $I$[b] | $I^c$ | $\ln(N_u/g)$[d] | $I$[b] | $I^c$ | $\ln(N_u/g)$[d] | $I$[b] | $I^c$ | $\ln(N_u/g)$[d] |
| 4-2 Q(9) | 1.498884 | 0.863(0.107) | 0.041(0.005) | 27.867(0.124) | ⋯ | ⋯ | ⋯ | ⋯ | ⋯ | ⋯ |
| 4-2 O(3) | 1.509865 | 5.782(0.311) | 0.275(0.015) | 31.156(0.054) | 4.432(0.269) | 0.372(0.024) | 30.890(0.061) | 2.731(0.224) | 0.511(0.044) | 30.406(0.082) |
| 5-3 Q(4) | 1.515792 | 2.356(0.229) | 0.112(0.011) | 30.306(0.097) | 1.737(0.168) | 0.146(0.014) | 30.001(0.096) | ⋯ | ⋯ | ⋯ |
| 3-1 O(5) | 1.522026 | 2.920(0.188) | 0.139(0.009) | 30.990(0.064) | 2.271(0.172) | 0.190(0.015) | 30.739(0.076) | 2.022(0.212) | 0.378(0.041) | 30.623(0.105) |
| 5-3 Q(5) | 1.528641 | 2.562(0.199) | 0.122(0.010) | 29.125(0.078) | 2.251(0.186) | 0.189(0.016) | 28.996(0.083) | 1.320(0.131) | 0.247(0.025) | 28.462(0.099) |
| 6-4 S(0) | 1.536908 | 1.942(0.150) | 0.092(0.007) | 30.600(0.077) | 2.134(0.156) | 0.179(0.013) | 30.694(0.073) | ⋯ | ⋯ | ⋯ |
| 10-7 O(3) | 1.548851 | 1.039(0.111) | 0.049(0.005) | 29.146(0.106) | 0.893(0.102) | 0.075(0.009) | 28.995(0.114) | 0.488(0.072) | 0.091(0.014) | 28.390(0.148) |
| 5-3 O(2) | 1.560730 | 2.524(0.169) | 0.120(0.008) | 31.481(0.067) | 1.876(0.138) | 0.157(0.012) | 31.184(0.073) | 1.113(0.114) | 0.208(0.022) | 30.662(0.103) |
| 5-3 Q(7) | 1.562627 | 1.578(0.120) | 0.075(0.006) | 28.402(0.076) | 1.285(0.098) | 0.108(0.008) | 28.196(0.076) | ⋯ | ⋯ | ⋯ |
| 4-2 O(4) | 1.563516 | 2.546(0.160) | 0.121(0.008) | 31.355(0.063) | 2.340(0.139) | 0.196(0.012) | 31.271(0.059) | 1.311(0.110) | 0.245(0.022) | 30.692(0.084) |
| 7-5 S(2) | 1.588290 | 1.240(0.113) | 0.059(0.005) | 29.124(0.091) | 0.973(0.097) | 0.082(0.008) | 28.881(0.100) | 0.860(⋯) | 0.161(⋯) | 28.758(⋯) |
| 6-4 Q(1) | 1.601535 | 3.992(0.193) | 0.190(0.010) | 30.248(0.048) | 3.369(0.173) | 0.283(0.015) | 30.078(0.051) | 2.222(0.134) | 0.416(0.028) | 29.662(0.060) |
| 6-4 Q(2) | 1.607386 | 3.813(0.194) | 0.182(0.010) | 31.136(0.051) | 2.255(0.157) | 0.189(0.014) | 30.611(0.070) | 1.600(0.138) | 0.299(0.027) | 30.268(0.086) |
| 5-3 O(3) | 1.613536 | 4.932(0.237) | 0.235(0.012) | 30.697(0.048) | 4.112(0.214) | 0.345(0.019) | 30.515(0.052) | 2.549(0.165) | 0.477(0.034) | 30.037(0.065) |
| 13-9 Q(1) | 1.614812 | 0.247(0.057) | 0.012(0.003) | 28.383(0.233) | ⋯ | ⋯ | ⋯ | ⋯ | ⋯ | ⋯ |
| 6-4 Q(3) | 1.616211 | 2.879(0.158) | 0.137(0.008) | 29.505(0.055) | 2.353(0.136) | 0.197(0.012) | 29.303(0.058) | 1.673(0.116) | 0.313(0.023) | 28.963(0.069) |
| 7-5 S(1) | 1.620530 | 2.723(0.145) | 0.130(0.007) | 29.208(0.053) | 2.283(0.143) | 0.191(0.013) | 29.032(0.063) | 1.098(0.116) | 0.205(0.022) | 28.300(0.106) |
| 4-2 O(5) | 1.622292 | 3.133(0.162) | 0.149(0.008) | 30.507(0.052) | 2.716(0.154) | 0.228(0.014) | 30.364(0.057) | 1.914(0.143) | 0.358(0.029) | 30.014(0.075) |
| 6-4 Q(4) | 1.628084 | 0.982(0.098) | 0.047(0.005) | 29.325(0.100) | 0.718(0.093) | 0.060(0.008) | 29.012(0.129) | 0.492(0.074) | 0.092(0.014) | 28.634(0.151) |
| 6-4 Q(5) | 1.643080 | 1.858(0.129) | 0.088(0.006) | 28.703(0.070) | 1.425(0.115) | 0.119(0.010) | 28.438(0.081) | 0.832(0.084) | 0.156(0.016) | 27.900(0.101) |
| 3-1 O(7) | 1.645324 | 0.668(0.068) | 0.032(0.003) | 29.871(0.102) | 0.615(0.065) | 0.052(0.006) | 29.789(0.106) | 0.353(0.051) | 0.066(0.010) | 29.233(0.145) |
| 11-8 Q(1) | 1.657105 | 0.730(0.083) | 0.035(0.004) | 28.851(0.114) | 0.570(0.075) | 0.048(0.006) | 28.604(0.131) | 0.545(0.066) | 0.102(0.013) | 28.558(0.122) |
| 7-5 S(0) | 1.658482 | 1.054(0.087) | 0.050(0.004) | 30.020(0.083) | 0.818(0.095) | 0.069(0.008) | 29.767(0.116) | ⋯ | ⋯ | ⋯ |
| 8-6 S(5) | 1.664578 | 0.518(0.075) | 0.025(0.004) | 26.994(0.144) | ⋯ | ⋯ | ⋯ | ⋯ | ⋯ | ⋯ |
| 5-3 O(4) | 1.671821 | 1.999(0.138) | 0.095(0.007) | 30.793(0.069) | 1.372(0.114) | 0.115(0.010) | 30.417(0.083) | 1.382(0.107) | 0.259(0.021) | 30.424(0.077) |
| 6-4 O(2) | 1.675019 | 2.127(0.128) | 0.101(0.006) | 31.167(0.060) | 1.451(0.102) | 0.122(0.009) | 30.784(0.071) | 1.125(⋯) | 0.211(⋯) | 30.530(⋯) |
| 4-2 O(6) | 1.686494 | 0.791(0.085) | 0.038(0.004) | 30.350(0.108) | ⋯ | ⋯ | ⋯ | ⋯ | ⋯ | ⋯ |
| 1-0 S(9) | 1.687721 | 1.017(0.108) | 0.048(0.005) | 29.014(0.106) | 0.610(0.081) | 0.051(0.007) | 28.504(0.133) | 0.205(0.045) | 0.038(0.008) | 27.415(0.218) |
| 8-6 S(3) | 1.701797 | 1.005(0.099) | 0.048(0.005) | 27.806(0.098) | 0.846(0.093) | 0.071(0.008) | 27.635(0.110) | 0.453(0.068) | 0.085(0.013) | 27.010(0.150) |
| 7-5 Q(1) | 1.728779 | 3.613(0.211) | 0.172(0.010) | 30.150(0.058) | 2.836(0.207) | 0.238(0.018) | 29.907(0.073) | 2.394(0.129) | 0.448(0.027) | 29.738(0.054) |
| 6-4 O(3) | 1.732637 | 4.227(0.233) | 0.201(0.011) | 30.382(0.055) | 3.519(0.212) | 0.295(0.019) | 30.199(0.060) | 1.776(0.129) | 0.332(0.026) | 29.515(0.073) |
| 5-3 O(5) | 1.735888 | 3.222(0.159) | 0.153(0.008) | 30.194(0.049) | 2.298(0.154) | 0.193(0.013) | 29.856(0.067) | ⋯ | ⋯ | ⋯ |
| 1-0 S(7) | 1.748035 | 3.624(0.218) | 0.173(0.011) | 29.937(0.060) | 2.475(0.204) | 0.208(0.018) | 29.555(0.082) | ⋯ | ⋯ | ⋯ |
| 4-2 O(7) | 1.756296 | 0.873(0.091) | 0.042(0.004) | 29.527(0.105) | 0.645(0.070) | 0.054(0.006) | 29.225(0.108) | 0.351(0.052) | 0.066(0.010) | 28.617(0.148) |
| 11-8 O(3) | 1.760929 | 0.940(0.100) | 0.045(0.005) | 29.124(0.106) | ⋯ | ⋯ | ⋯ | ⋯ | ⋯ | ⋯ |
| 7-5 O(5) | 2.022040 | 1.022(0.078) | 0.049(0.004) | 28.774(0.076) | 0.972(0.073) | 0.082(0.006) | 28.724(0.075) | 0.247(0.031) | 0.046(0.006) | 27.356(0.124) |
| 6-4 O(7) | 2.029694 | 0.415(0.043) | 0.020(0.002) | 28.161(0.104) | ⋯ | ⋯ | ⋯ | ⋯ | ⋯ | ⋯ |
| 1-0 S(2) | 2.033756 | 9.052(0.224) | 0.431(0.012) | 32.560(0.025) | 5.579(0.174) | 0.468(0.017) | 32.076(0.031) | 2.795(0.118) | 0.523(0.026) | 31.385(0.042) |
| 8-6 O(3) | 2.041816 | 1.613(0.113) | 0.077(0.005) | 29.450(0.070) | 1.436(0.103) | 0.120(0.009) | 29.333(0.072) | 0.835(0.077) | 0.156(0.015) | 28.790(0.093) |
| 3-2 S(5) | 2.065557 | 1.335(0.096) | 0.064(0.005) | 28.924(0.072) | 0.971(0.078) | 0.081(0.007) | 28.606(0.081) | 0.518(0.049) | 0.097(0.010) | 27.978(0.095) |
| 12-9 O(3) | 2.069969 | 0.311(0.037) | 0.015(0.002) | 28.392(0.118) | 0.289(0.035) | 0.024(0.003) | 28.321(0.122) | ⋯ | ⋯ | ⋯ |
| 2-1 S(3) | 2.073510 | 7.288(0.179) | 0.347(0.010) | 30.693(0.025) | 4.718(0.141) | 0.396(0.014) | 30.258(0.030) | 2.258(0.109) | 0.423(0.023) | 29.521(0.048) |
| 9-7 Q(3) | 2.100659 | 0.387(0.034) | 0.018(0.002) | 27.915(0.088) | ⋯ | ⋯ | ⋯ | ⋯ | ⋯ | ⋯ |
| 8-6 O(4) | 2.121570 | 0.610(0.044) | 0.029(0.002) | 29.429(0.072) | 0.540(0.045) | 0.045(0.004) | 29.307(0.083) | 0.220(0.025) | 0.041(0.005) | 28.409(0.114) |
| 1-0 S(1) | 2.121831 | 21.002(0.291) | 1.000 | 32.734(0.014) | 11.924(0.219) | 1.000 | 32.168(0.018) | 5.343(0.146) | 1.000 | 31.366(0.027) |
| 2-1 S(2) | 2.154225 | 4.197(0.137) | 0.200(0.007) | 31.509(0.033) | 2.683(0.114) | 0.225(0.010) | 31.061(0.043) | 1.388(0.081) | 0.260(0.017) | 30.402(0.058) |
| 9-7 O(2) | 2.172704 | 0.317(0.035) | 0.015(0.002) | 29.556(0.109) | 0.341(0.032) | 0.029(0.003) | 29.627(0.095) | 0.079(0.012) | 0.015(0.002) | 28.169(0.156) |

8

**Table 1**
(Continued)

| Line | $\lambda$[a] | Region A | | | Region B | | | Region C | | |
|---|---|---|---|---|---|---|---|---|---|---|
| | | $I$[b] | $I$[c] | $\ln(N_u/g)$[d] | $I$[b] | $I$[c] | $\ln(N_u/g)$[d] | $I$[b] | $I$[c] | $\ln(N_u/g)$[d] |
| 4-3 S(5) | 2.200951 | 0.748(0.048) | 0.036(0.002) | 28.743(0.064) | ... | ... | ... | ... | ... | ... |
| 3-2 S(3) | 2.201397 | 2.869(0.107) | 0.137(0.005) | 29.841(0.037) | 2.043(0.091) | 0.171(0.008) | 29.501(0.045) | 0.797(0.056) | 0.149(0.011) | 28.560(0.070) |
| 1-0 S(0) | 2.223299 | 8.990(0.199) | 0.428(0.011) | 33.685(0.022) | 5.215(0.152) | 0.437(0.015) | 33.140(0.029) | 2.736(0.108) | 0.512(0.025) | 32.495(0.040) |
| 2-1 S(1) | 2.247721 | 8.546(0.213) | 0.407(0.012) | 31.532(0.025) | 5.767(0.174) | 0.484(0.017) | 31.139(0.030) | 2.974(0.121) | 0.557(0.027) | 30.477(0.041) |
| 9-7 O(3) | 2.253719 | 1.102(0.073) | 0.052(0.004) | 29.279(0.067) | 0.725(0.055) | 0.061(0.005) | 28.861(0.076) | 0.547(0.059) | 0.102(0.011) | 28.578(0.107) |
| 3-2 S(2) | 2.287026 | 1.813(0.096) | 0.086(0.005) | 30.719(0.053) | 1.424(0.080) | 0.119(0.007) | 30.477(0.056) | 0.854(0.067) | 0.160(0.013) | 29.967(0.078) |
| 10-8 Q(2) | 2.337306 | 0.233(0.029) | 0.011(0.001) | 29.200(0.124) | ... | ... | ... | ... | ... | ... |
| 4-3 S(3) | 2.344479 | 1.273(0.076) | 0.061(0.004) | 29.298(0.060) | 0.733(0.053) | 0.061(0.005) | 28.745(0.072) | 0.345(0.039) | 0.065(0.007) | 27.992(0.112) |
| 2-1 S(0) | 2.355629 | 3.663(0.224) | 0.174(0.011) | 32.468(0.061) | 2.545(0.187) | 0.213(0.016) | 32.104(0.073) | 1.564(0.148) | 0.293(0.029) | 31.617(0.095) |
| 1-0 Q(1) | 2.406594 | 34.941(0.471) | 1.664(0.032) | 34.005(0.013) | 17.513(0.331) | 1.469(0.039) | 33.314(0.019) | 8.191(0.235) | 1.533(0.061) | 32.554(0.029) |
| 1-0 Q(2) | 2.413436 | 11.449(0.317) | 0.545(0.017) | 33.827(0.028) | 7.547(0.247) | 0.633(0.024) | 33.410(0.033) | 3.608(0.175) | 0.675(0.038) | 32.672(0.048) |
| 1-0 Q(3) | 2.423731 | 18.537(0.476) | 0.883(0.026) | 32.964(0.026) | 10.166(0.352) | 0.853(0.033) | 32.363(0.035) | 4.886(0.246) | 0.914(0.052) | 31.630(0.050) |
| 1-0 Q(4) | 2.437491 | 6.285(0.212) | 0.299(0.011) | 32.783(0.034) | 5.074(0.182) | 0.426(0.017) | 32.569(0.036) | 3.774(0.181) | 0.706(0.039) | 32.273(0.048) |

**Notes.**
[a] The wavelengths are in units of $\mu$m.
[b] The intensity has been corrected for extinction in units of $10^{-19}$ W m$^{-2}$ arcsec$^{-2}$. Uncertainties are written in parentheses.
[c] The normalized intensity with respect to the intensity of 1-0 S(1). Uncertainties are given in parentheses.
[d] Extinction corrected upper-level column density in units of $\ln(\text{cm}^{-2})$.

**Table 2**
Dynamical Information from $H_2$ Lines

| Line | Region A | | | | | Region B | | | | | Region C | | | | |
|---|---|---|---|---|---|---|---|---|---|---|---|---|---|---|---|
| | $V_{shift}$[a] (kms$^{-1}$) | $V_{LSR}$[b] (kms$^{-1}$) | $\Delta V_{obs}$[c] (kms$^{-1}$) | $\Delta V_{inst}$[d] (kms$^{-1}$) | $\Delta V_{fwhm}$[e] (kms$^{-1}$) | $V_{shift}$[a] (kms$^{-1}$) | $V_{LSR}$[b] (kms$^{-1}$) | $\Delta V_{obs}$[c] (kms$^{-1}$) | $\Delta V_{inst}$[d] (kms$^{-1}$) | $\Delta V_{fwhm}$[e] (kms$^{-1}$) | $V_{shift}$[a] (kms$^{-1}$) | $V_{LSR}$[b] (kms$^{-1}$) | $\Delta V_{obs}$[c] (kms$^{-1}$) | $\Delta V_{inst}$[d] (kms$^{-1}$) | $\Delta V_{fwhm}$[e] (kms$^{-1}$) |
| 4-2 O(3) | −18.63 | 3.90 | ⋯ | ⋯ | ⋯ | −18.69 | 3.83 | ⋯ | ⋯ | ⋯ | −18.88 | 3.64 | 7.20 | 7.02 | 1.62 |
| 5-3 Q(4) | −18.47 | 4.05 | ⋯ | ⋯ | ⋯ | −19.02 | 3.50 | 8.10 | 7.04 | 4.01 | −18.44 | 4.08 | 8.59 | 7.04 | ⋯ |
| 3-1 O(5) | −17.57 | 4.96 | ⋯ | ⋯ | ⋯ | ⋯ | ⋯ | ⋯ | ⋯ | ⋯ | −19.04 | 3.48 | ⋯ | ⋯ | ⋯ |
| 10-7 O(3) | −19.24 | 3.28 | ⋯ | ⋯ | ⋯ | −19.65 | 2.87 | ⋯ | ⋯ | ⋯ | −20.28 | 2.25 | ⋯ | ⋯ | ⋯ |
| 4-2 O(4) | −19.17 | 3.35 | ⋯ | ⋯ | ⋯ | −19.13 | 3.39 | ⋯ | ⋯ | ⋯ | ⋯ | ⋯ | ⋯ | ⋯ | ⋯ |
| 6-4 Q(1) | −18.96 | 3.56 | ⋯ | ⋯ | ⋯ | −19.00 | 3.52 | ⋯ | ⋯ | ⋯ | −18.61 | 3.92 | 7.89 | 7.37 | 2.82 |
| 6-4 Q(5) | −18.66 | 3.86 | 8.80 | 7.54 | 4.53 | −18.60 | 3.92 | 8.90 | 7.54 | 4.72 | −18.80 | 3.72 | 8.55 | 7.54 | 4.04 |
| 11-8 Q(1) | −18.74 | 3.78 | ⋯ | ⋯ | ⋯ | −18.86 | 3.66 | 8.03 | 7.60 | 2.59 | ⋯ | ⋯ | ⋯ | ⋯ | ⋯ |
| 5-3 O(4) | −20.28 | 2.24 | ⋯ | ⋯ | ⋯ | −18.80 | 3.73 | ⋯ | ⋯ | ⋯ | −19.87 | 2.65 | 7.98 | 7.66 | 2.24 |
| 11-8 Q(3) | −18.05 | 4.47 | ⋯ | ⋯ | ⋯ | −18.93 | 3.59 | ⋯ | ⋯ | ⋯ | ⋯ | ⋯ | ⋯ | ⋯ | ⋯ |
| 8-6 S(3) | −17.51 | 5.01 | 8.91 | 7.80 | 4.31 | ⋯ | ⋯ | ⋯ | ⋯ | ⋯ | ⋯ | ⋯ | ⋯ | ⋯ | ⋯ |
| 8-6 S(2) | −17.90 | 4.63 | 9.26 | 7.92 | 4.80 | ⋯ | ⋯ | ⋯ | ⋯ | ⋯ | ⋯ | ⋯ | ⋯ | ⋯ | ⋯ |
| 5-3 O(5) | −18.84 | 3.68 | 8.09 | 7.95 | 1.47 | −18.80 | 3.73 | ⋯ | ⋯ | ⋯ | ⋯ | ⋯ | ⋯ | ⋯ | ⋯ |
| 1-0 S(2) | −18.19 | 4.33 | 9.32 | 6.97 | 6.18 | ⋯ | ⋯ | ⋯ | ⋯ | ⋯ | −17.96 | 4.57 | ⋯ | ⋯ | ⋯ |
| 9-7 Q(3) | −18.87 | 3.66 | ⋯ | ⋯ | ⋯ | −19.86 | 2.67 | 7.14 | 6.89 | ⋯ | −20.46 | 2.06 | ⋯ | ⋯ | ⋯ |
| 1-0 S(1) | −19.02 | 3.51 | 8.53 | 6.87 | 5.06 | −19.15 | 3.37 | 7.72 | 6.87 | 3.52 | −19.02 | 3.50 | 7.70 | 6.87 | 3.49 |
| 9-7 O(2) | −17.82 | 4.70 | 8.36 | 6.81 | 4.85 | −18.55 | 3.97 | 7.48 | 6.81 | 3.09 | ⋯ | ⋯ | ⋯ | ⋯ | ⋯ |
| 3-2 S(3) | −19.84 | 2.68 | 8.37 | 6.77 | 4.93 | ⋯ | ⋯ | ⋯ | ⋯ | ⋯ | −19.99 | 2.53 | 8.03 | 6.77 | 4.31 |
| 2-1 S(1) | −20.15 | 2.38 | 7.62 | 6.72 | 3.59 | −19.99 | 2.54 | 7.30 | 6.72 | 2.84 | −19.63 | 2.89 | 7.59 | 6.72 | 3.53 |
| 9-7 O(3) | −19.02 | 3.50 | ⋯ | ⋯ | ⋯ | −19.50 | 3.02 | 7.11 | 6.71 | 2.35 | −19.87 | 2.66 | ⋯ | ⋯ | ⋯ |
| 3-2 S(2) | ⋯ | ⋯ | ⋯ | ⋯ | ⋯ | ⋯ | ⋯ | ⋯ | ⋯ | ⋯ | −18.76 | 3.77 | 7.31 | 6.68 | 2.97 |
| 1-0 Q(1) | −19.38 | 3.15 | 8.48 | 6.55 | 5.39 | ⋯ | ⋯ | ⋯ | ⋯ | ⋯ | ⋯ | ⋯ | ⋯ | ⋯ | ⋯ |
| 1-0 Q(2) | −19.67 | 2.85 | 8.98 | 6.54 | 6.16 | ⋯ | ⋯ | ⋯ | ⋯ | ⋯ | ⋯ | ⋯ | ⋯ | ⋯ | ⋯ |
| 1-0 Q(3) | −20.13 | 2.40 | 7.82 | 6.53 | 4.31 | −18.42 | 4.10 | 7.27 | 6.53 | 3.19 | −17.34 | 5.18 | 7.56 | 6.53 | 3.81 |
| 1-0 Q(4) | −19.19 | 3.33 | ⋯ | ⋯ | ⋯ | ⋯ | ⋯ | ⋯ | ⋯ | ⋯ | ⋯ | ⋯ | ⋯ | ⋯ | ⋯ |

**Notes.**
[a] The velocity shift measured from the best-fit Gaussian.
[b] The velocity shift corrected by the Earth and heliocentric velocities of 8.63 and 13.89 km s$^{-1}$ at the time of the observation.
[c] The observed FWHM line width of the $H_2$ emission lines without deconvolving the instrument profile.
[d] The FWHM line width of the instrument profile, assuming it is Gaussian.
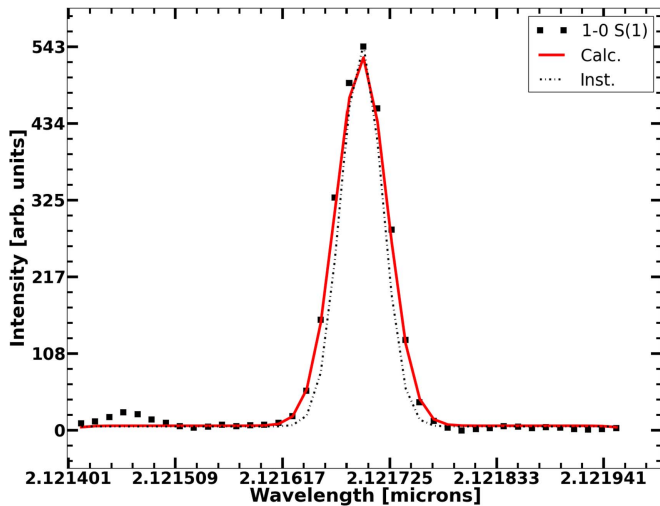[e] The FWHM resolved line width of the $H_2$ emission lines.

**Figure 5.** Observed $H_2$ 1-0 S(1) line profile from region A in black squares. The black dotted points present the instrument profile. The solid red line is from the convolution of the instrument profile and the derived intrinsic line width.

$0.34\,\mathrm{km\,s^{-1}}$, $3.29 \pm 0.26\,\mathrm{km\,s^{-1}}$, and $3.20 \pm 0.27\,\mathrm{km\,s^{-1}}$, respectively. Those values correspond to the upper limits of the kinematic temperatures of $\sim$930, $\sim$470, and $\sim$440 K, if all gas motions are thermal. Our derived line widths are consistent with the published result from Lemaire et al. (1999) for the 1-0 S(1) line, $3.4 \pm 0.8\,\mathrm{km\,s^{-1}}$.

## 4. Results

### 4.1. $H_2$ Line Ratios

The ratio of the line intensity, 2-1 S(1)/1-0 S(1), is commonly used to discriminate between excitation of molecular hydrogen by collisional excitation and excitation by FUV photons (e.g., Hayashi et al. 1985; Black & Van Dishoeck 1987; Burton 1992).

In the case of fluorescent excitation in a low-density PDR ($n_{H_2} < 5 \times 10^4$ cm$^{-3}$), the 2-1 S(1)/1-0 S(1) ratio is $\sim$0.56 (see, for example, Model 14 of Black & Van Dishoeck 1987). In denser PDR regions or shocked regions (e.g., bipolar outflows), where collisional excitations populate the $\nu = 0$ and $\nu = 1$ levels, the ratio is $\sim$0.08 (e.g., Model S2 in Black & Van Dishoeck 1987). From our data, the ratio of 2-1 S(1)/1-0 S(1) was $0.41 \pm 0.01$, $0.48 \pm 0.02$, and $0.56 \pm 0.03$ in regions A, B, and C, respectively. The $H_2$ level populations in region A are somewhat more affected by collisional excitation than those in region C and the gradient in the ratios implies a gradient in the gas density.

Our measured ratios of 2-1 S(1)/1-0 S(1) are different from the case of $H_2$ emissions, which are characterized by shock excitations (Burton et al. 1988, 1989). In the case of shocked regions, e.g., the shock driven by a supernova remnant (SNR), IC 443 (Richter et al. 1995), the values of the 2-1 S(1)/1-0 S(1) ratio are $\sim$0.06–0.2. In addition, Oh et al. (2016a, 2016b) also measured the ratio of 2-1 S(1)/1-0 S(1), $\sim$0.05–0.14, in LKH$\alpha$ 234 and Orion KL outflow regions. From our data, the ratios of 2-1 S(1)/1-0 S(1) are larger than those in the cases of shocked regions such as IC 443, LKH$\alpha$ 234 and Orion KL outflow regions.

### 4.2. Ortho-to-para Ratio

Ortho $H_2$ (rovibrational states of odd $J$) has a total nuclear spin of 1, while para $H_2$ (even $J$) has a total nuclear spin of 0. The OPR of molecular hydrogen $H_2$ is the ratio of the total column density of ortho $H_2$ to that of para $H_2$, divided by the degeneracy $g_J$ (Hasegawa et al. 1987; Tanaka et al. 1989).

When $H_2$ is formed on the grain surface, the OPR initially has a value of 3. Radiative processes in $H_2$ consist of electric quadrupole transitions of $\Delta J = 0, \pm2$. Therefore, the original OPR cannot be changed by radiative processes. However, over time OPR can be altered by an exchange reaction of $H_2$ with other gas constituents such as atomic hydrogen and $H^+$ (Burton 1992; Sternberg & Neufeld 1999). The rates of this reaction are strongly dependent on the temperature. At a high temperature of $T \geqslant 200$ K, the value of the OPR is expected to be 3. Otherwise, in the case of lower temperature, $T \leqslant 200$ K, the OPR has lower values ($<$3) since more $H_2$ is formed in a para rotational state, $J = 0$ (Sternberg & Neufeld 1999).

Low OPRs ($<$1.8) has been observed in PDRs (e.g., Hasegawa et al. 1987; Fuente et al. 2000; Habart et al. 2011). Sternberg & Neufeld (1999) argued that differential self-shielding of ortho and para $H_2$ can affect the observed OPR. Due to optical depth effects, the FUV pumping rate of ortho $H_2$ is reduced, and the observed OPR will be lower than the actual value (Sternberg & Neufeld 1999). In shock regions, the OPRs are expected to be at or near the statistical equilibrium value of 3. But in some cases low OPRs ($<$3) are also observed (HH 54: Neufeld et al. 1998; SNRs: Hewitt et al. 2009). Low OPRs in shocked regions could be explained by scenarios in which these SNRs are interacting with a cold and quiescent cloud. On the other hand, the shock timescale is not long enough for the OPR of the shock excited gas to reach the equilibrium value (Wilgenbus et al. 2000; Hewitt et al. 2009).

Studies in the literature show that the OPR has values from 1–1.8 in $H_2$ fluorescent regions (e.g., Tanaka et al. 1989; Chrysostomou et al. 1993; Fuente et al. 2000). Initial evidence indicated that the OPR had a value different from 3 in NGC 2023 (Hasegawa et al. 1987). These authors estimated the OPR to be 1.4–2.0. Tanaka et al. (1989) found similar results suggesting that OPR had a value less than 3 in PDRs. Chrysostomou et al. (1993) found that OPR $= 1.8 \pm 0.5$ for M17. Habart et al. (2011) estimated an OPR of 1.8 for NGC 2023. Fuente et al. (2000) found that the OPR varies from 1.5 to 3 for NGC 7023.

Using the method described in Chrysostomou et al. (1993), we derived the OPR for NGC 7023 at three regions along the IGRINS slit. Table 3 and Figure 6 show the OPR as a function of the upper-level energy. Figure 6 shows the OPR values of regions A, B, and C. The average OPR was $1.82 \pm 0.11$, $1.75 \pm 0.09$, and $1.63 \pm 0.12$ for regions A, B, and C, respectively. Our derived OPR values are lower than that of Martini et al. (1997), who presented an OPR of $2.5 \pm 0.3$ for the northern filament of NGC 7023. In the calculation of Martini et al. (1997), they used one pair of upper state populations of the vibrational level $\nu = 1$ and $J = 3$–4. Martini et al. (1997) observed the NW part of NGC 7023 at $40\rlap{.}{''}0$ west, $34\rlap{.}{''}0$ north of the central star, which is offset $10''$ to the north from ours. Based on the argument of Sternberg & Neufeld (1999), the FUV pumping rate of para $H_2$ is reduced by optical depth effects. Therefore, the derived OPR of Martini et al. (1997) and this study is just a lower limit for the true value of

**Table 3**
Ortho-to-para Ratio as a Function of Vibrational Level

| Upper energy level (K)[a] | Ortho $H_2$ | Para $H_2$ | OPR region A[b] | OPR region B | OPR region C |
|---|---|---|---|---|---|
| 6310 | 1-0 Q(1) | 1-0 Q(2) | 2.15(0.09) | 1.72(0.09) | 1.65(0.13) |
| 6310 | 1-0 Q(1) | 1-0 S(0) | 2.48(0.10) | 2.25(0.12) | 1.97(0.15) |
| 6711 | 1-0 S(1) | 1-0 Q(2) | 2.15(0.06) | 1.72(0.06) | 1.65(0.08) |
| 6711 | 1-0 Q(3) | 1-0 Q(2) | 1.62(0.06) | 1.32(0.06) | 1.33(0.09) |
| 7268 | 1-0 S(1) | 1-0 S(2) | 1.31(0.07) | 1.33(0.08) | 1.15(0.10) |
| 7268 | 1-0 S(1) | 1-0 Q(4) | 1.05(0.12) | 0.81(0.09) | 0.47(0.08) |
| 7268 | 1-0 Q(3) | 1-0 Q(4) | 2.59(0.13) | 1.80(0.10) | 1.16(0.09) |
| 7268 | 1-0 Q(3) | 1-0 S(2) | 3.24(0.07) | 2.95(0.08) | 2.83(0.11) |
| 12322 | 2-1 S(1) | 2-1 S(0) | 1.56(0.15) | 1.54(0.18) | 1.33(0.20) |
| 12850 | 2-1 S(1) | 2-1 S(2) | 2.11(0.08) | 2.19(0.11) | 2.11(0.15) |
| 13520 | 2-1 S(3) | 2-1 S(2) | 2.11(0.07) | 2.18(0.09) | 2.11(0.12) |
| 18102 | 3-1 O(5) | 3-2 S(2) | 2.35(0.13) | 2.24(0.15) | 2.30(0.31) |
| 18736 | 3-2 S(3) | 3-2 S(2) | 2.35(0.10) | 2.24(0.10) | 2.30(0.10) |
| 22216 | 4-2 O(3) | 4-2 O(4) | 1.89(0.19) | 1.66(0.16) | 1.93(0.24) |
| 22556 | 4-2 O(5) | 4-2 O(4) | 1.89(0.10) | 1.66(0.10) | 1.93(0.16) |
| 26670 | 5-3 O(3) | 5-3 O(2) | 1.52(0.16) | 1.76(0.20) | 1.80(0.28) |
| 28188 | 5-3 Q(5) | 5-3 Q(4) | 1.66(0.14) | 1.76(0.16) | ... |
| 27183 | 5-3 O(5) | 5-3 O(4) | 2.23(0.14) | 2.54(0.18) | ... |
| 27626 | 5-3 O(5) | 5-3 Q(4) | 1.80(0.15) | 1.54(0.16) | ... |
| 31002 | 6-4 Q(1) | 6-4 O(2) | 1.43(0.14) | 1.77(0.20) | 1.45(...) |
| 31183 | 6-4 Q(1) | 6-4 Q(2) | 0.87(0.07) | 1.23(0.13) | 1.24(0.15) |
| 31482 | 6-4 Q(3) | 6-4 Q(2) | 0.99(0.06) | 1.39(0.09) | 1.23(0.12) |

**Notes.**
[a] The average value of the upper-level energy of ortho and para $H_2$.
[b] Uncertainties are written in parentheses.

the OPR. From the comparison between our derived OPR with that of Martini et al. (1997), we see that the OPR varies from ∼1.6 to 2.5 across the PDR region.

### 4.3. $H_2$ Column Density

Molecular $H_2$ emission lines are optically thin because they have small radiative transition probabilities. We present the level column densities divided by the level degeneracy $g_J$ against upper-level energy $E_u(\nu, J)/k$ in Table 1. Figure 7 shows the excitation diagrams of molecular $H_2$ emission lines in regions A, B, and C, respectively.

These excitation diagrams clearly reveal the $H_2$ excitation mechanism. For thermally excited $H_2$, the excitation diagram would show a single smooth function of $\ln N(\nu, J)$ against $E_u(\nu, J)$. In the case of fluorescent excitation, the plot shows a characteristic sawtooth distribution, where vibrational temperatures are much larger than rotational temperatures but each rotational ladder is characterized by a temperature that increases with increasing $J$ (e.g., Hasegawa et al. 1987; Tanaka et al. 1989; Burton 1992; Chrysostomou et al. 1993; Ramsay et al. 1993; Draine & Bertoldi 1996; Rosenthal et al. 2000). Figure 7 shows sawtooth distributions, which clearly indicate that the $H_2$ emission lines are mostly UV-excited.

## 5. Discussion

### 5.1. Comparison of the $H_2$ Spectra to a PDR Model

To investigate the physical conditions in the observed region, we compare the observed emission lines to PDR models from the literature. The large number of $H_2$ emission lines in
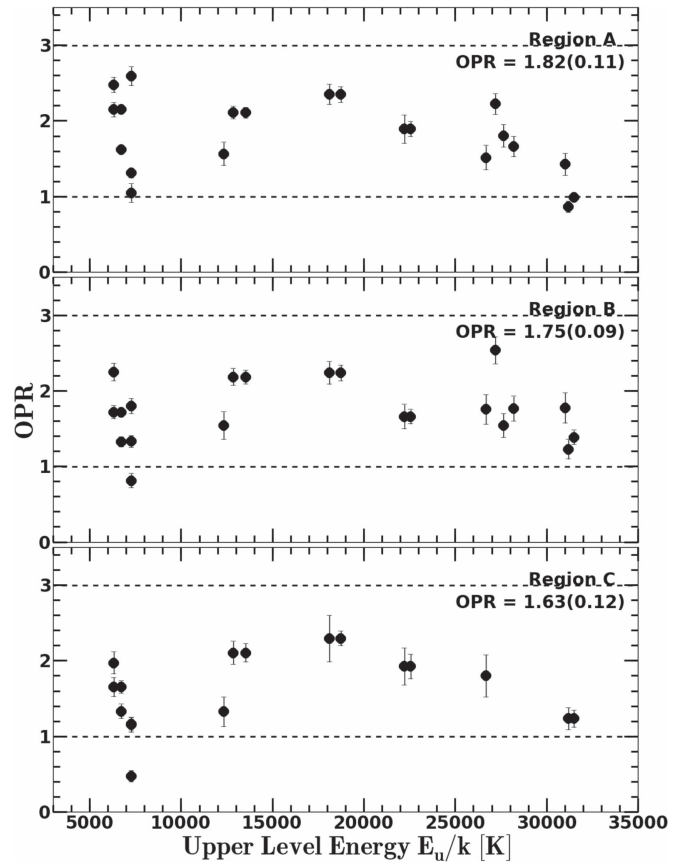


**Figure 6.** Plots of the OPR as a function of vibrational levels of regions A, B, and C. The dashed lines indicate the OPRs of 1 and 3. The text in the plots indicates the average OPRs of each region.
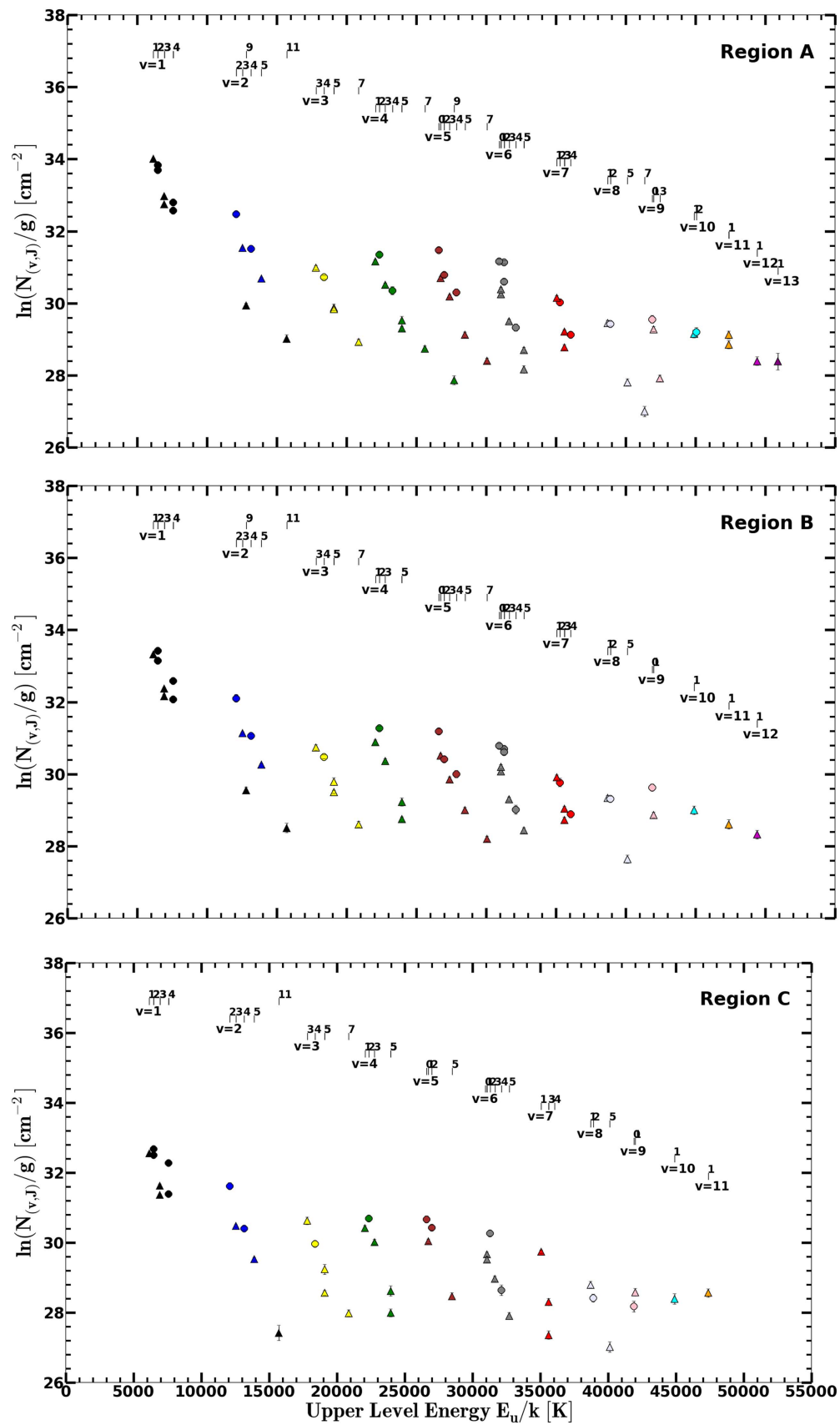
**Figure 7.** Excitation diagram of the $H_2$ level column density distribution for region A (the top plot). The observed column densities have been corrected for extinction, $A_V = 2.2$ mag. The column densities have been divided by the level degeneracies, assuming the ortho-to-para ratio is 3. The circles and triangles present the ortho and para $H_2$, respectively. The middle and bottom plots are same as the top plot, except for the spectra in region B and C, respectively.

**Table 4**
Gas Density from Comparison of the Line Ratios with the PDR Model of
Draine & Bertoldi ([1996](#))

| Model | $n_H$ (cm$^{-3}$) | UV field strength [Habing] | $\chi^{2a}$ | $\chi^{2b}$ | $\chi^{2c}$ |
|-------|-------------------|----------------------------|-------------|-------------|-------------|
| aw3o | $10^2$ | 1 | 77 | 23 | 29 |
| bw3d | $10^2$ | 10 | 91 | 26 | 31 |
| Bw3o | $10^3$ | 10 | 86 | 25 | 30 |
| Cw3o | $10^3$ | $10^2$ | 52 | 16 | 26 |
| Gw3o | $10^4$ | $10^2$ | 25 | 15 | 26 |
| Hw3o | $10^4$ | $10^3$ | 26 | 17 | 27 |
| Lw3o | $10^5$ | $10^3$ | 32 | 38 | 39 |
| Mw3o | $10^5$ | $10^4$ | 57 | 53 | 48 |
| Qw3o | $10^6$ | $10^4$ | 75 | 85 | 63 |

**Notes.**
[a] $\chi^2$ of region A.
[b] $\chi^2$ of region B.
[c] $\chi^2$ of region C.

the IGRINS spectrum of NGC 7023 allows us to compare observed line strengths with the PDR models in detail. Here we compare the line ratios of all observed $H_2$ emission lines to the PDR model of Draine & Bertoldi ([1996](#); hereafter DB96). DB96 provides $H_2$ emission lines at densities from $10^2$ to $10^6$ cm$^{-3}$ and UV field intensities from 1 $G_0$ to $10^4$ $G_0$. The $A_V$ value used in Section [3.2](#) is the stellar extinction value, and the nebula extinction value may differ from that. Martini et al. ([1997](#), [1999](#)) agree that this variation of this extinction value by a factor of 2 does not affect their results. We also test how the line ratio of 2-1 S(1)/1-0 S(1) varies while changing the extinction value of $A_V$ by $\Delta A_V = \pm 2$ mag. Our results show that the line ratio varies within $\pm 0.01$ with changing the extinction value, which has no meaningful effect on our calculations.

The best fits are determined from the minimum reduced chi-squared value of the differences between the line ratios in the model and those in the data. Table [4](#) shows the derived reduced chi-squared values between the observed data and the models. Those chi-squared values are fitted again with a curve to find the minimum in between the models. The best fits are at $n_H = 10^{4.55 \pm 0.24}$ cm$^{-3}$, $10^{3.25 \pm 0.40}$ cm$^{-3}$, and $10^{3.09 \pm 0.53}$ cm$^{-3}$ for regions A, B, and C respectively. Figure [8](#) shows how we derive the densities from the minimum reduced chi-squared values. Using low spectral resolution NIR $H_2$ emission lines, Martini et al. ([1997](#), [1999](#)) found that the NW filament of NGC 7023 has a high-density clump of $n_H \sim 10^6$ cm$^{-3}$ in the filament with a lower density of $10^4$–$10^5$ cm$^{-3}$. By using radio emission lines from *ISO* observations, Fuente et al. ([2000](#)) found that the NW filament has a high-density filament of $n_H \sim 10^6$ cm$^{-3}$ immersed in a diffuse interfilament of $n_H \sim 10^4$ cm$^{-3}$. Köhler et al. ([2014](#)) estimated the density values for the NW filament of $n_H = 10^4$–$10^6$ cm$^{-3}$ using CO emission from *Spitzer* observations.

Figure [9](#) shows the normalized $H_2$ level column density distributions of the observational data and the calculation of model DB96 for regions A, B, and C. In region A, we display the model Lw30 of DB96, which has a density of $n_H = 10^5$ cm$^{-3}$. In regions B and C, we use the model Hw30, which has $n_H = 10^4$ cm$^{-3}$. The UV intensity of both DB96 models is $G = 10^3$ $G_0$. Both models have densities that
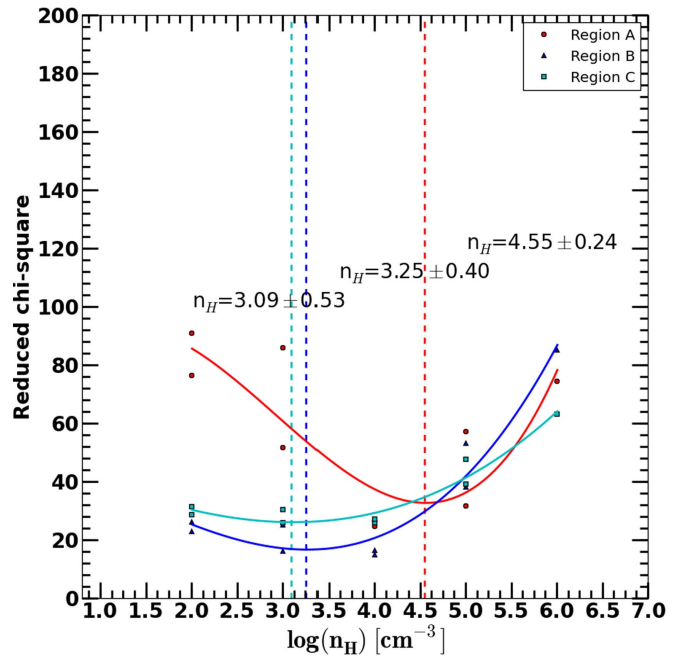


**Figure 8.** Estimated densities of regions A (red), B (blue), and C (cyan) from DB96. The solid lines display the fitting of reduced chi-squared values of regions A, B, and C. The dashed lines show the minimum reduced chi-squared values from the fitting.

are close to those values, determined from the best-fit lines using the reduced chi-squared method discussed above. The gas temperature assumed in the models, $T_{gas} = 500$ K, is close to the temperature that we estimated using the $H_2$ line widths in Section [3.3](#).

For the $H_2$ level populations, Figure [9](#) shows good agreement between the model predictions and the observational data for all vibrational excited levels of $\nu = 1$–13. Although the agreement is good for all vibrational levels, there are significant differences (by factors of 2–3) between the model results and the observed data for the $H_2$ emission lines in $\nu = 1$ and rotational states $J = 9$ and 11. This discrepancy may come from the uncertainty in the rovibrational distribution function $\delta(\upsilon, J)$ of newly formed $H_2$ assumed in the model. In the model of DB96, the $H_2$ emission lines arising from low-$J$ states are not sensitive to the distribution of newly formed $H_2$. However, the lines at high-$J$ levels are affected by the function of $\delta(\upsilon, J)$. The emission from high-$J$ levels ($J \geqslant 7$) will increase by a factor of $\sim 2$ when the formation temperature varies from 2000 K to $5 \times 10^4$ K. In the models of Lw30 and Hw3o, the author assumed that the newly formed $H_2$ has a formation temperature of $T_f = 5 \times 10^4$ K. From the comparison between the model calculations with our observed data, we expected that the formation temperature for newly formed $H_2$ would be lower, around $T_f = 1 \times 10^3$–$2 \times 10^3$ K.

To date, the level distribution of newly formed $H_2$ is unclear. The nature of the grain surface controls the properties and the formation process of newly formed $H_2$ molecules. Depending on the grain surface formational conditions, $H_2$ molecules may be formed in (low-$\nu$ and high-$J$ levels) or (high-$\nu$ and low-$J$ levels; e.g., Hunter & Waston [1978](#); Duley & Williams [1986](#)).
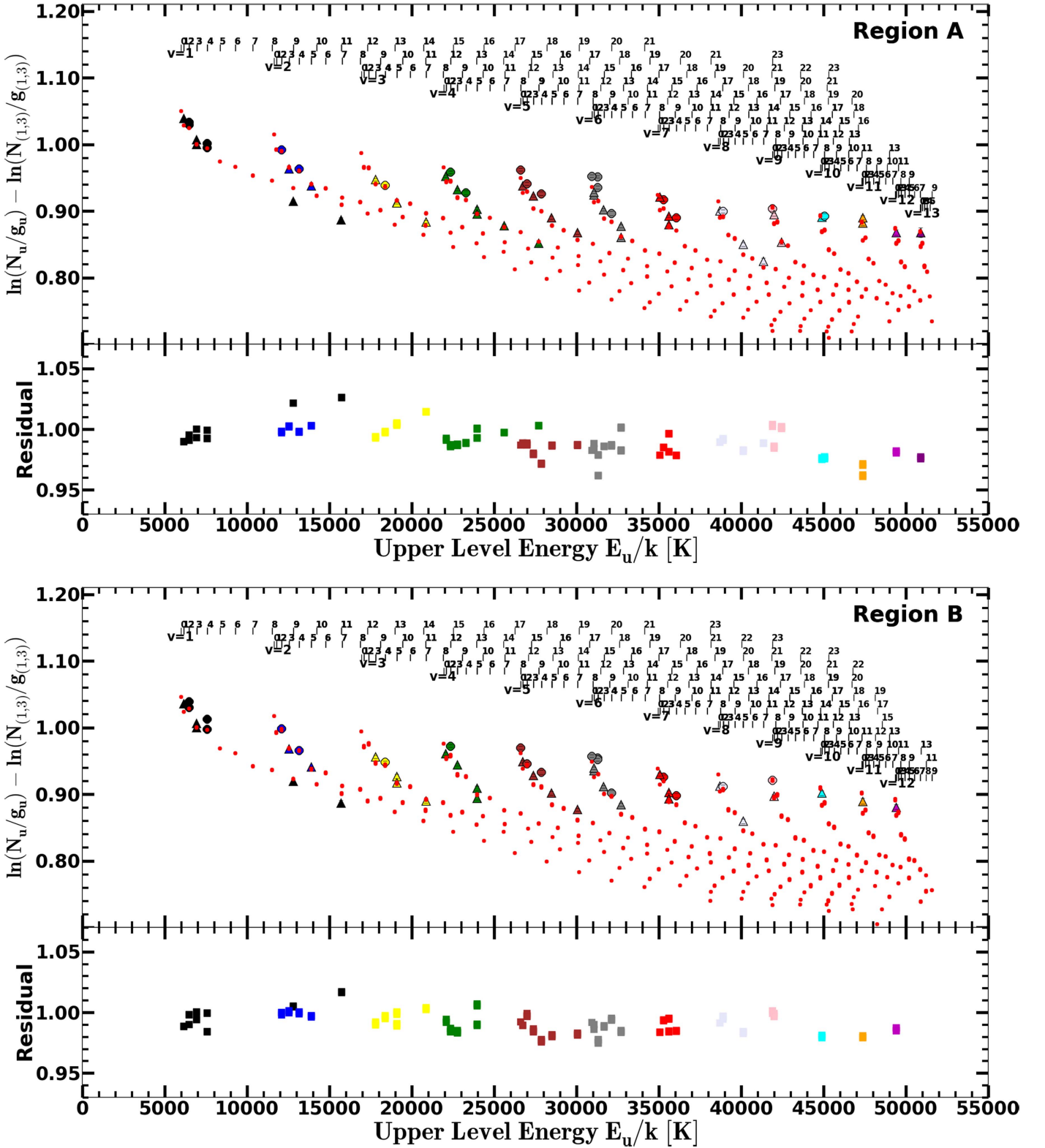
**Figure 9.** Comparison of the normalized H2 level column density distributions of the observational data and the calculation of model DB96 for regions A, B, and C. The H2 level column density distributions are similarly displayed as in Figure 7. The red circles represent the model calculation of DB96. For region A, the model is Lw3o, with $nH = 10^5$ cm$^{-3}$ and $G = 10^3 G^0$. In the cases of region B and C, the model is Hw3o, with $nH = 10^4$ cm$^{-3}$ and $G = 10^3 G^0$. The bottom panel in each plot displays the residual values between the model results and the observational data.

In addition, Burton (1992) and Burton et al. (2002) argued that they may have detected newly formed H$_2$ in $\nu = 4$ and 6 levels based on the H$_2$ observations of the reflection nebula NGC 2023 and the northern bar of the M17. In our results, we report that the level distribution of newly formed H$_2$ may be in the levels of $\nu = 1$ and $J \geqslant 9$.
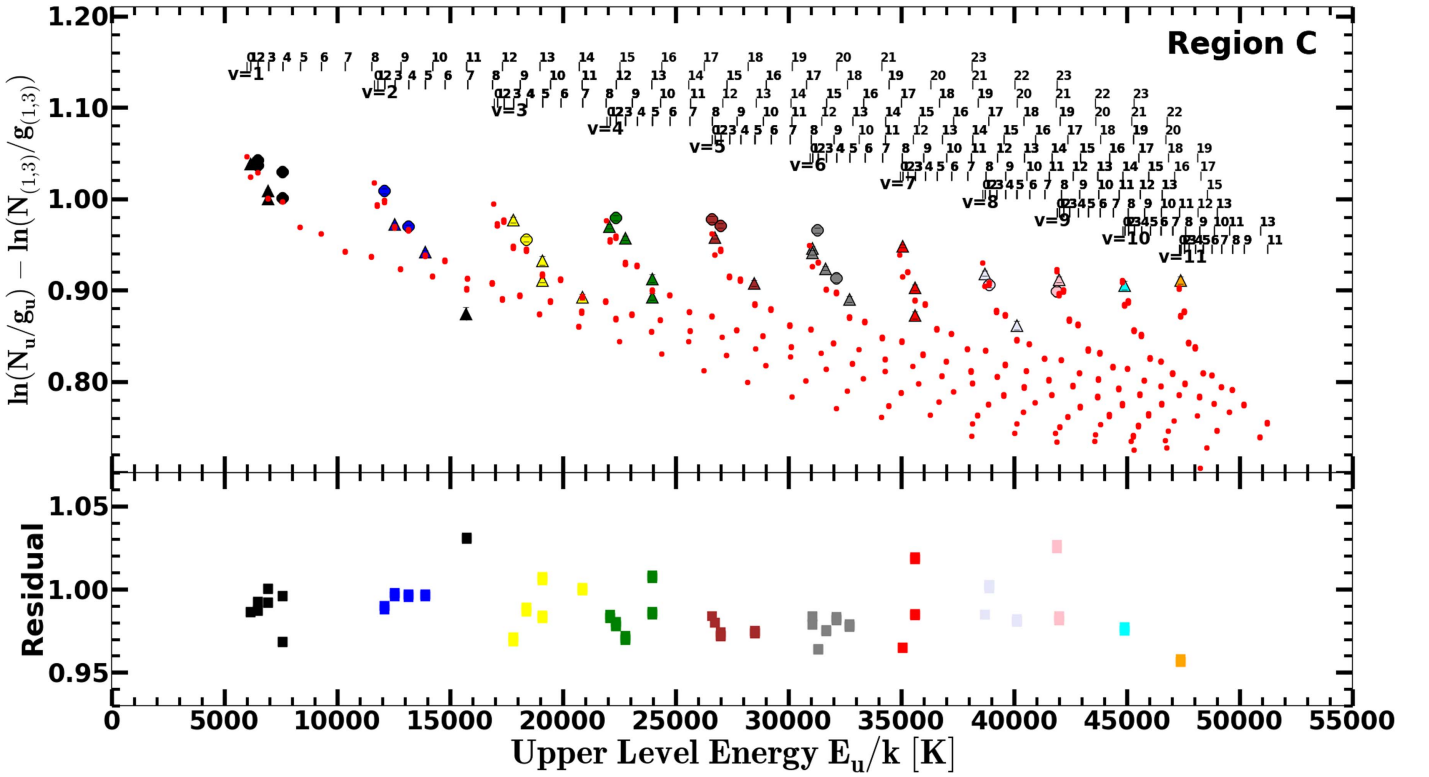
**Figure 9.** (Continued.)

## 5.2. An Advancing Photodissociation Front to the Molecular Cloud

The gradient of both the temperature and the OPR supports the idea that the PDR front is moving, as previously discussed by Fuente et al. (1999, 2000) based on a non-equilibrium OPR for the gas with a kinetic temperature at 400 K and a gradient of the OPR across the PDR of NGC 7023. The authors discussed that the existence of an advancing PDR front is the most likely explanation for this behavior. In that scenario, the PDR is interacting continuously via the cool gas of the molecular cloud, in which the equilibrium OPR is lower than 3. The gas that was recently incorporated into the PDR is predicted to have an OPR lower than the equilibrium value, and also has the lowest temperature. The OPR will increase and reach values close to 3 at higher temperatures.

In Section 3.3, our results indicated a gradient in the kinetic temperature between ∼400 and ∼900 K from regions B and C to region A. In Section 4.2, we found that the OPR increases from ∼1.6 to 2.5 across the PDR region. Moreover, Lemaire et al. (1999) found a velocity gradient in the molecular species in the PDR. We confirmed an offset in the velocity of $H_2$ ($V_{LSR} = 3.50 \pm 0.16 \, \text{km s}^{-1}$) relative to other molecular species (e.g., CO line) in the PDR region. Our results confirm the argument of Fuente et al. (1999, 2000) that the observed region is an advancing PDR front relative to the molecular cloud.

## 5.3. Size of the $H_2$ Clumps

We found a variation in density distribution throughout regions A, B, and C within the observational area of $1'' \times 15''$. The gas density is higher in region A and decreases toward regions B and C. In Figure 10, the top plot shows the density profile of regions A, B, and C (in each area of $1'' \times 5''$, corresponding to a spatial scale of 0.01 pc). The bottom plot displays the estimated densities, covering an area of $1'' \times 1''$, corresponding to a scale of 0.002 pc. We see variations of the density within each region. In particular, the density distribution in region A varies from $10^{5.03\pm0.32}$ to $10^{4.18\pm0.32} \, \text{cm}^{-3}$ within ∼0.01 pc. Across region A, the variation of density distribution shows two peaks of densities. One peak has a density of $10^{5.03\pm0.32} \, \text{cm}^{-3}$, and the other is $10^{4.67\pm0.24} \, \text{cm}^{-3}$. The gradients of the density distribution may indicate evidence of a high-density clump with a size smaller than ∼$5 \times 10^{-3}$ pc.

Through the variations of density distribution, we found clumpy structures in the observed area, including a high-density clump of $n_H \sim 10^5 \, \text{cm}^{-3}$ with a size of ∼$5 \times 10^{-3}$ pc or less, embedded in the lower-density regions of $n_H = 10^3$–$10^4 \, \text{cm}^{-3}$. Previous works have argued that the clump sizes are $10^{-3}$–$10^{-4}$ pc (Churchwell et al. 1987; Garay et al. 1987). Sellgren et al. (1992) also found that NGC 7023 has a clumpy structure. The clump size that we derive is consistent with the previous report from Lemaire et al. (1996). Using a high spatial resolution $0''8$ for the $H_2$ 1-0 S(1) and 1-0 S(2) observations from the NW of NGC 7023, the authors found that there is evidence of small-scale structures on a scale size of 3 to $4 \times 10^{-3}$ pc.

The increasing density on small scales may also be evidence of local turbulence in the region, which has important connections to the star formation processes. These rapid changes of density within the region, on subparsec scales, give us a glimpse into where new stars are formed. A typical size-scale for a region where stars are born is within "core" sizes of 0.03–0.2 pc, with a mean density of $10^4$–$10^5 \, \text{cm}^{-3}$ (Bergin & Tafalla 2007; Ward-Thompson et al. 2007; Kennicutt & Evans 2012).
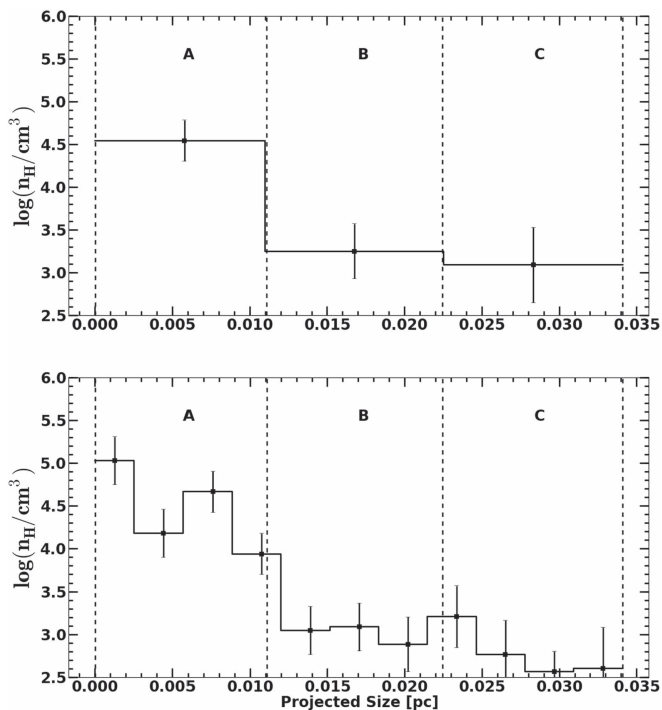
**Figure 10.** The top plot displays the estimated densities of regions A, B, and C (spatial resolution of $\sim 5''$ or 0.01 pc) from the PDR model of DB96. The solid line shows the estimate densities by DB96. The bottom plot presents the estimated densities of DB96 with a spatial resolution of $\sim 1''$ or 0.002 pc.

## 6. Summary and Conclusion

We analyzed the near-infrared $H_2$ emission lines from the $1'' \times 15''$ region in the NW filament of the reflection nebula, NGC 7023. The high spatial and spectral resolutions of IGRINS provide many $H_2$ rovibrational emission lines, which we have used to resolve the physical structure of the PDR, and look into details of the physical excitation mechanisms of the observed regions. We summarize our results as follows.

The diagnostic ratios of 2-1 S(1)/1-0 S(1) in regions A, B, and C are between 0.41–0.56. The ratios indicate that regions B and C are mostly UV-excited, while the excitation mechanism in region A is partially a product of collisional excitation or collisional de-excitation. The derived OPR of 1.63–1.82 also indicates that the observed $H_2$ lines are UV fluorescence. In addition, the distributions of the excitation diagrams confirm that the detected $H_2$ emission lines are from PDR.

The features of the gradient of kinetic temperature, velocity, and OPR of $H_2$ emission lines in the observed areas demonstrate the presence of the dynamic PDR front relative to the molecular cloud.

We found the gradient density distribution within the observed regions. We suggest that the area has a clumpy structure, including a high-density clump of $\sim 10^5$ cm$^{-3}$ with a size smaller than $\sim 5 \times 10^{-3}$ pc, that is embedded in lower-density regions of $10^3$–$10^4$ cm$^{-3}$, closer to the Herbig B3Ve $-$B5 star HD 200775.

## References

Afşar, M., Sneden, C., Frebel, A., et al. 2016, ApJ, 819, 103
Alecian, E., Catala, C., Wade, G. A., et al. 2008, MNRAS, 385, 391
Alecian, E., Wade, G. A., Catala, C., et al. 2013, MNRAS, 429, 1001
Allers, K. N., Jaffe, D. T., Lacy, J. H., Draine, B. T., & Richter, M. J. 2005, ApJ, 630, 368A
An, J. H., & Sellgren, K. 2003, ApJ, 599, 312
Baschek, B., Beltrametti, M., Kóppen, J., & Traving, G. 1982, A&A, 105, 300
Bergin, E. A., & Tafalla, M. 2007, ARA&A, 45, 339
Bertoldi, F., Draine, B. T., Rosenthal, D., et al. 2000, in IAU Symp. 197, Astrochemistry: From Molecular Clouds to Planetary Systems, ed. Y. C. Minh & E. G. van Dishoeck (San Francisco, CA: ASP), 191
Bertoldi, F., Timmermann, R., Rosenthal, D., Drapatz, S., & Wright, C. M. 1999, A&A, 346, 267
Black, J. H., & Van Dishoeck, E. F. 1987, ApJ, 322, 412
Burton, M., Bulmer, M., Moorhouse, A., Geballe, T. R., & Brand, P. W. J. L. 1992, MNRAS, 257, 1
Burton, M. G. 1992, AuJPh, 45, 463
Burton, M. G., Brand, P. W. J. L., Geballe, T. R., & Webster, A. S. 1989, MNRAS, 236, 409
Burton, M. G., Geballe, T. R., Brand, P. W. J. L., & Webster, A. S. 1988, MNRAS, 231, 617
Burton, M. G., Howe, J. E., Geballe, T. R., & Brand, J. L. 1998, PASA, 15, 194
Burton, M. G., Londish, D., & Brand, P. W. J. L. 2002, MNRAS, 333, 721
Chokshi, A., Tielens, A. G. G. M., Werner, M. W., & Castelaz, M. W. 1988, ApJ, 334, 803
Chrysostomou, A., Brand, P. W. J. L., Burton, M. G., & Moorhouse, A. 1992, MRAS, 256, 528
Chrysostomou, A., Brand, P. W. J. L., Burton, M. G., & Moorhouse, A. 1993, MRAS, 265, 329
Chrysostomou, A., Brand, P. W. J. L., Ramsay-Howat, S. K. R., & Burton, M. G. 1998, in ASP Conf. Ser., Star Formation with Infrared Space Observatory, ed. J. L Yuh & R. Liseau (San Francisco, CA: ASP), 330
Churchwell, E., Wood, D. O. S., Felli, M., & Massi, M. 1987, ApJ, 321, 516
Cox, A. N. 2000, Allen's Astrophysical Quantities (New York: AIP Press)
Draine, B. T., & Bertoldi, F. 1996, ApJ, 468, 269
Draine, B. T., & Bertoldi, F. 1999, in ESA-SP 427, The Universe as Seen by ISO, ed. P. Cox & M. F. Kessler (Noordwijk: ESA), 553
Duley, W. W., & Williams, D. A. 1986, MNRAS, 223, 177
Fleming, B., France, K., Lupu, R. E., & McCandliss, S. R. 2010, ApJ, 725, 159
Fuente, A., Martín-Pintado, J., Cernicharo, J., & Gerin, M. 2000, A&A, 354, 1053
Fuente, A., Martín-Pintado, J., Neri, R., Rogers, C., & Moriarty-Schieven, G. 1996, A&A, 310, 286
Fuente, A., Martín-Pintado, J., Rodriguez-Fernandez, N. J., et al. 1999, ApJL, 518, L45
Garay, G., Moran, J. M., & Reid, M. J. 1987, ApJ, 314, 535
Gatley, I., Hasegawa, T., Suzuki, H., et al. 1987, ApJL, 318, L73
Habart, E., Abergel, A., Boulanger, F., et al. 2011, A&A, 527, A122

Habart, E., Boulanger, F., Verstraete, L., Walmsley, C. M., & Pineau des Forêts, G. 2004, A&A, 414, 531
Hasegawa, T., Gatley, I., Garden, R. P., et al. 1987, ApJ, 318, 77
Hayashi, M., Hasegawa, T., Gatley, I., et al. 1985, MNRAS, 215, 31P
Hewitt, J. W., Rho, J., Andersen, M., & Reach, W. T. 2009, ApJ, 694, 1266
Hollenbach, D. J., & Tielens, A. G. G. M. 1999, RvMP, 71, 173
Hora, J. L., & Latter, W. B. 1996, ApJ, 461, 288
Hunter, D. A., & Waston, W. D. 1978, ApJ, 226, 447
Kaplan, K. F., Dinerstein, H. L., Oh, H., et al. 2017, ApJ, 838, 152
Kennicutt, R. C., Jr., & Evans, N. J., II 2012, ARA&A, 50, 531
Kessler, M. F., Steinz, J. A., Anderegg, M. E., et al. 1996, A&A, 315, L27
Köhler, M., Habart, E., Arab, H., et al. 2014, A&A, 569, 109
Le, H. A. N., Pak, S., Jaffe, D. T., et al. 2015, AdSpR, 55, 2509
Lee, J.-E., Park, S., Green, J. D., et al. 2015, ApJ, 807, 84
Lee, J.-J. 2015, plp, Zenodo, Version 2.0, doi:10.5281/zenodo.18579
Lee, S., Lee, J.-E., Park, S., et al. 2016, ApJ, 826, 179
Lee, S., & Pak, S. 2006, JKAS, 39, 151
Lemaire, J. L., Field, D., Gerin, M., et al. 1996, A&A, 308, 895
Lemaire, J. L., Field, D., Maillard, J. P., et al. 1999, A&A, 349, 253
Luhman, K. L., Engelbracht, C. W., & Luhman, M. L. 1998, ApJ, 499, 799
Luhman, K. L., & Rieke, G. H. 1996, ApJ, 461, 298
Luhman, M. L., Jaffe, D. T., Sternberg, A., Herrmann, F., & Poglitsch, A. 1997, ApJ, 482, 298
Marquez-Lugo, R. A., Guerrero, M. A., Ramos-Larios, G., & Miranda, L. F. 2015, MNRAS, 453, 1888
Martini, P., Sellgren, K., & Depoy, D. L. 1999, ApJ, 526, 772
Martini, P., Sellgren, K., & Hora, J. L. 1997, ApJ, 484, 296
Mathis, J. S. 1990, ARA&A, 28, 37
McCartney, M. S. K., Brand, P. W. J. L., Burton, M. G., & Chrysostomou, A. 1999, MNRAS, 307, 315
Neufeld, D. A., Melnick, G. J., & Harwit, M. 1998, ApJL, 506, L75
Oh, H., Pyo, T.-S., Kaplan, K., et al. 2016b, ApJ, 833, 275
Oh, H., Pyo, T.-S., Yuk, I.-S., et al. 2016a, ApJ, 817, 148
Park, C., Jaffe, D. T., Yuk, I.-S., et al. 2014, Proc. SPIE, 9147, 91471D
Pilleri, P., Joblin, C., Boulanger, F., & Onaka, T. 2012a, A&A, 577, A16
Pilleri, P., Montillaud, J., Berne, O., & Joblin, C. 2012b, A&A, 542, 69
Ramsay, S. K., Chrysostomou, A., Geballe, T. R., Brand, P. W. J. L., & Mountain, M. 1993, MNRAS, 263, 695

Richter, M. J., Graham, J. R., & Wright, G. S. 1995, ApJ, 454, 277
Rosenthal, D., Bertoldi, F., & Drapatz, S. 2000, A&A, 356, 705
Rousselot, P., Lidman, C., Moreels, G., & Monnet, G. 2000, A&A, 354, 1134
Sellgren, K. 1986, ApJ, 305, 399
Sellgren, K., Werner, M. W., & Dinerstein, H. L. 1992, ApJ, 400, 238S
Shaw, G., Ferland, G. J., Abel, N. P., Stancil, P. C., & van Hoof, P. A. M. 2004, ApJ, 624, 794
Shaw, G., Ferland, G. J., Henney, W. J., et al. 2009, ApJ, 701, 677
Sheffer, Y., & Wolfire, M. G. 2013, ApJL, 774, L14
Sheffer, Y., Wolfire, M. G., Hollenbach, D. J., Kaufman, M. J., & Cordier, M. 2011, ApJ, 741, 45
Sim, C. K., Le, H. A. N., Pak, S., et al. 2014, AdSpR, 53, 11
Sterling, N. C., Dinerstein, H. L., Kaplan, K. F., & Bautista, M. A. 2016, ApJL, 819, L9
Sternberg, A., & Dalgarno, A. 1989, ApJ, 338, 197
Sternberg, A., & Neufeld, D. A. 1999, ApJ, 516, 371
Takami, M., Usada, T., Sugai, H., et al. 2000, ApJ, 529, 268
Tanaka, M., Hasegawa, T., Hayashi, S. S., Brand, P. W. J. L., & Gatley, I. 1989, ApJ, 336, 207
Thi, W. F., van Dishoeck, E. F., Black, J. H., et al. 1999, in ESA-SP 427, The Universe as Seen by ISO, ed. P. Cox & M. F. Kessler (Noordwijk: ESA), 767
Tielens, A. G. G. M., & Hollenbach, D. J. 1985a, ApJ, 291, 772
Tielens, A. G. G. M., & Hollenbach, D. J. 1985b, ApJ, 291, 747
Timmermann, R., Bertoldi, F., Wright, C. M., et al. 1996, A&A, 315, L281
van den Ancker, M. E., Thé, P. S., Tjin A Djie, H. R. E., et al. 1997, A&A, 324, L33
Ward-Thompson, D., André, P., Crutcher, R., et al. 2007, in Protostars and Planets V, ed. B. Reipurth, D. Jewitt, & K. Keil (Tucson, AZ: Univ. Arizona Press), 33
Weingartner, J. C., & Draine, B. T. 1999, in ESA-SP 427, The Universe as Seen by ISO, ed. P. Cox & M. F. Kessler (Noordwijk: ESA), 783
Wilgenbus, D., Cabrit, S., Pineau des Forêts, G., & Flower, D. R. 2000, A&A, 356, 1010
Witt, A. N., & Cottrell, M. J. 1980, ApJ, 235, 899
Witt, A. N., Gordon, K. D., Vijh, U. P., et al. 2006, ApJ, 636, 303
Yuk, I.-S., Jaffe, D. T., Barnes, S., et al. 2010, Proc SPIE, 7735, 77351M